NASA/TM—2015-218720

Capillary Channel Flow (CCF) EU2–02 on the International Space Station (ISS): An Experimental Investigation of Passive Bubble Separations in an Open Capillary Channel

Mark M. Weislogel, Andrew P. Wollman, Ryan M. Jenson, John T. Geile, John F. Tucker, Brentley M. Wiles, Andy L. Trattner, and Claire DeVoe
Portland State University, Portland, Oregon

Lauren M. Sharp
Glenn Research Center, Cleveland, Ohio

Peter J. Canfield, Joerg Klatte, and Michael E. Dreyer
University of Bremen, Bremen, Germany

June 2015

NASA STI Program . . . in Profile

Since its founding, NASA has been dedicated to the advancement of aeronautics and space science. The NASA Scientific and Technical Information (STI) Program plays a key part in helping NASA maintain this important role.

The NASA STI Program operates under the auspices of the Agency Chief Information Officer. It collects, organizes, provides for archiving, and disseminates NASA's STI. The NASA STI Program provides access to the NASA Technical Report Server—Registered (NTRS Reg) and NASA Technical Report Server—Public (NTRS) thus providing one of the largest collections of aeronautical and space science STI in the world. Results are published in both non-NASA channels and by NASA in the NASA STI Report Series, which includes the following report types:

- TECHNICAL PUBLICATION. Reports of completed research or a major significant phase of research that present the results of NASA programs and include extensive data or theoretical analysis. Includes compilations of significant scientific and technical data and information deemed to be of continuing reference value. NASA counter-part of peer-reviewed formal professional papers, but has less stringent limitations on manuscript length and extent of graphic presentations.

- TECHNICAL MEMORANDUM. Scientific and technical findings that are preliminary or of specialized interest, e.g., "quick-release" reports, working papers, and bibliographies that contain minimal annotation. Does not contain extensive analysis.

- CONTRACTOR REPORT. Scientific and technical findings by NASA-sponsored contractors and grantees.

- CONFERENCE PUBLICATION. Collected papers from scientific and technical conferences, symposia, seminars, or other meetings sponsored or co-sponsored by NASA.

- SPECIAL PUBLICATION. Scientific, technical, or historical information from NASA programs, projects, and missions, often concerned with subjects having substantial public interest.

- TECHNICAL TRANSLATION. English-language translations of foreign scientific and technical material pertinent to NASA's mission.

For more information about the NASA STI program, see the following:

- Access the NASA STI program home page at http://www.sti.nasa.gov

- E-mail your question to help@sti.nasa.gov

- Fax your question to the NASA STI Information Desk at 757-864-6500

- Telephone the NASA STI Information Desk at 757-864-9658

- Write to:
  NASA STI Program
  Mail Stop 148
  NASA Langley Research Center
  Hampton, VA 23681-2199

NASA/TM—2015-218720

Capillary Channel Flow (CCF) EU2–02 on the International Space Station (ISS): An Experimental Investigation of Passive Bubble Separations in an Open Capillary Channel

Mark M. Weislogel, Andrew P. Wollman, Ryan M. Jenson, John T. Geile, John F. Tucker, Brentley M. Wiles, Andy L. Trattner, and Claire DeVoe
Portland State University, Portland, Oregon

Lauren M. Sharp
Glenn Research Center, Cleveland, Ohio

Peter J. Canfield, Joerg Klatte, and Michael E. Dreyer
University of Bremen, Bremen, Germany

National Aeronautics and
Space Administration

Glenn Research Center
Cleveland, Ohio 44135

June 2015

Acknowledgments

Support for this work is shared by the National Aeronautics and Space Administration cooperative agreement NNX09AP66A and the German Federal Ministry of Economics and Technology (BMWi) via the German Aerospace Center (DLR) under Grant No. 50WM1145. Special thanks are due to astronaut Chris Cassidy for installation of CCF–EU2–2 on the ISS. We also wish to thank Portland State University personnel W.H. Blackmore, Y. Chen, P.M. Weislogel, and D. Burns, Astrium Engineering, and the NASA cadre at Glenn Research Center including R. Green, Johnson Space Center, and especially the MSG crew and cadre at Marshall Space Flight Center. A.P. Wollman is supported in part through NASA/Oregon Space Grant Consortium Grant NNX10AK68H, C. DeVoe through the NSF REU summer program, and A. Trattner as a summer student from Lincoln High School.

Level of Review: This material has been technically reviewed by technical management.

Available from

NASA STI Program
Mail Stop 148
NASA Langley Research Center
Hampton, VA 23681-2199

National Technical Information Service
5285 Port Royal Road
Springfield, VA 22161
703-605-6000

This report is available in electronic form at http://www.sti.nasa.gov/ and http://ntrs.nasa.gov/

Abstract

It would be significantly easier to design fluid systems for spacecraft if the fluid phases behaved similarly to those on earth. In this research an open 15.8° wedge-sectioned channel is employed to separate bubbles from a two-phase flow in a microgravity environment. The bubbles appear to rise in the channel and coalesce with the free surface in much the same way as would bubbles in a terrestrial environment, only the combined effects of surface tension, wetting, and conduit geometry replace the role of buoyancy. The host liquid is drawn along the channel by a pump and noncondensible gas bubbles are injected into it near the channel vertex at the channel inlet. Control parameters include bubble volume, bubble frequency, liquid volumetric flow rate, and channel length. The asymmetrically confined bubbles are driven in the cross-flow direction by capillary forces until they at least become inscribed within the section or until they come in contact with the free surface, whereupon they usually coalesce and leave the flow. The merging of bubbles enhances, but does not guarantee, the latter. The experiments are performed aboard the International Space Station as a subset of the Capillary Channel Flow experiments. The flight hardware is commanded remotely and continuously from ground stations during the tests and an extensive array of experiments is conducted identifying numerous bubble flow regimes and regime transitions depending on the ratio and magnitude of the gas and liquid volumetric flow rates. The breadth of the publicly available experiments is conveyed herein primarily by narrative and by regime maps, where transitions are approximated by simple expressions immediately useful for the purposes of design and deeper analysis.

1 Introduction

Separation of bubbles from a liquid medium is a critical, but non-trivial task aboard spacecraft due to the absence of a net gravitational force that precludes using buoyancy as a strong separation mechanism. Though any number of methods are pursued to replace the role of gravity in the multi-phase fluid systems of spacecraft, the ever-present capillary force which exploits the combination of surface tension, wetting, and system geometry provides a natural and often passive solution. In Fig. 1 is sketched an open wedge channel in a zero-gravity environment along which a steady forced liquid flows at flow rate Q_l. The free surface profile adjusts so that its local capillary pressure balances the convective and viscous pressure losses along the channel. Bubbles introduced upstream near the channel vertex are asymmetrically confined by the planar side walls of the wedge and through a combination of mechanisms the bubbles are forced in a cross-stream direction away from the vertex until they reach approximately inscribed elevations. If the bubbles are large enough, the channel long enough, and the liquid flow rate low enough, there will be ample time for the bubbles to reach the free surface, coalesce, and leave the flow. In doing so, this simple conduit geometry performs a passive bubble separation operation in an analogous manner to simple bubble rise in a buoyant open channel flow.

When occurring in the nearly weightless environment of an orbiting spacecraft,

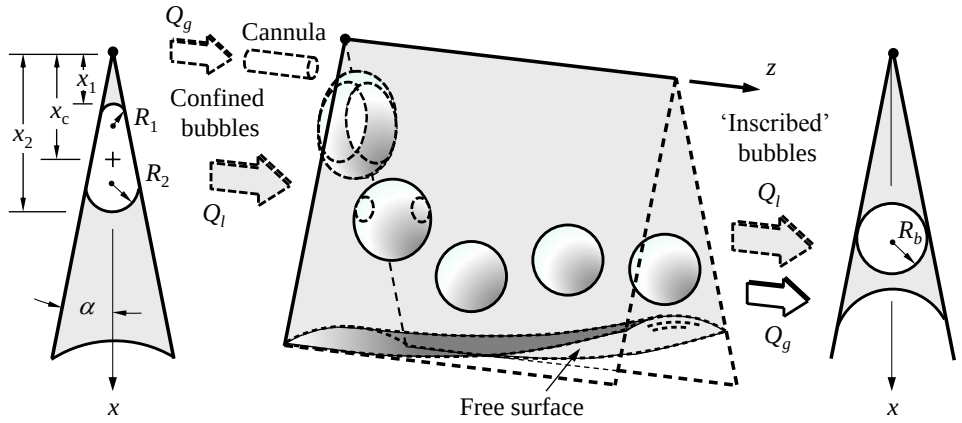

Figure 1. Sketch of an open wedge channel with liquid flow Q_l left to right and with gas flow Q_g bubbles injected near the vertex at channel inlet. The free surface deflects inward to resist inertial and viscous pressure losses along the channel. Capillary pressure gradients drive the bubble away from the vertex toward the free surface. The bubbles are also convected downstream, eventually reaching an elevation in the channel where they are approximately inscribed. Idealized section views at the channel entrance and exit are depicted at left and right, respectively.

such processes possess unique characteristics attributable to the large length scale capillary phenomena possible there: The flows are often inertial with highly underdamped low frequency free surfaces, the evidence of buoyancy on unconfined bubble motion is truly negligible, and capillary flow rates increase by many orders of magnitude ($\sim 10^6$-fold), as do various dimensionless groups including the ratio of surface roughness to characteristic container length ($\sim 10^3$-fold). Regarding research, the larger length scale systems allow accurate construction of increasingly complex containers and conduits consisting of transparent materials with full optical access. Regarding applications, the demonstration of nearly full scale systems in the relevant reduced-gravity environment increases technology readiness levels adding confidence to both spacecraft technology developers and adopters. Terrestrial research along such lines is extensive, but naturally limited to milli-to-microscale systems where viscous forces play a significant role—the majority of work focusing on confined bubbles in symmetric geometries such as circular tubes, parallel plates, and rectangular channels (i.e., [1]). Significant progress concerning the hydrodynamics of bubbles in shear flows is reported and reviewed by [2]. For a sample of terrestrial microfluidic bubble separation and generation methods see [3], [4], [5], [6], [7], and in particular for the wedge geometry see [8] and [9].

For a quiescent liquid, the fundamental problem of asymmetrically-confined bubble migration in a wedge is addressed in terrestrial experiments by [10] and [11] and in drop tower experiments by [12]. The passive migration of such bubbles through a forced convective flow is introduced by [8] and [9] with recent experiments also performed in the microgravity environment reported by [12]. The analytic approach

to the problem often begins from the simplified sketch at left in Fig. 1, where in the narrow wedge half-angle limit $\alpha \ll 1$ the bubble is approximated as a modulated disc-like body characterized by radii of curvature R_1, R_2, and R_c (a 'squeezed bubble' according to [10] and an 'air puddle' according to [11]). Because $R_1 < R_2$, the capillary under-pressure in the liquid at the narrower end of the bubble is lower than that of the broader end, and the resulting pressure gradient drives the liquid upward displacing the bubble downward.

Employing a genetic algorithm to a force balance on such a bubble, [10] consider the impact of liquid viscosity, partial wetting and contact line pinning, dynamic contact angle, and the presence of thin films on the inertia of the 'bubble' (via the liquid). For their laminar flows, Metz et al. find that viscous resistance dominates the flow near the vertex when the bubble is more or less a modulated disc and velocities are high. Dynamic contact line affects arising from local viscous normal stresses play a more important role as velocities decrease and the bubble eventually achieves a more spherical shape.

Using an energy balance, [11] employs the same narrow wedge limit $\alpha \ll 1$ with $2x_c/(x_2 - x_1) \ll 1$ to find the transient bubble center migration position x_c in two distinct viscous regimes: a near-vertex regime where

$$x_c \approx \frac{\sigma\alpha}{3\mu} t \tag{1}$$

and a contact line dissipation regime far from the vertex

$$x_c \approx \left(\frac{13}{8 \cdot 2^{1/2} \chi^{3/2}} \frac{\sigma}{\mu} \left(\frac{V_b}{2\pi\alpha} \right)^{3/4} t \right)^{4/13}, \tag{2}$$

where σ, μ, V_b, and t are the liquid surface tension, liquid dynamic viscosity, bubble volume, and time, and $\chi = 1.1$ is a viscous resistance coefficient. The investigations of both Metz et al. and Reyssat do well to predict accompanying data.

As systems increase in size, inertial forces dominate viscous resistance and the simplified schematic of Fig. 1 gives way to more complex behavior. Fig. 2 provides images of a sealed wedge vessel that is mounted to an experiment rig which is placed inside a drag shield and dropped 21.6 m in a drop tower providing a low-gravity test duration of 2.1 s, [13]. Here, a wedge conduit of acute included angle $2\alpha = 15.5°$ is shown oriented vertex upward though tilted with respect to $\mathbf{g}$ at angle $0 \leq \gamma \leq 90°$ with a bubble of known volume centered and balanced. The tilt angle γ allows further control of the initial condition. Release of the experiment into free fall reduces the body force by a factor of $\sim 10^{-5}$ and the asymmetrically confined bubble is driven downward by capillary forces.

In Fig. 3 are presented five such passive capillarity-driven bubble migration experiments performed in a drop tower. The bubble volume and fluid types are listed for each example shown. Relevant nominal thermophysical properties for 10 cs polydimethylsiloxane (PDMS) are density $\rho = 953$ kg/m^3, dynamic viscosity $\mu = 0.00935$ kg/m·s, surface tension $\sigma = 0.0201$ N/m, contact angle $\theta = 0°$, and index of refraction $N_d = 1.399$. Such properties for Novec HFE-7500 are $\rho = 1614$ kg/m^3, $\mu = 0.00125$ kg/m·s, $\sigma = 0.0162$ N/m, $\theta = 0°$, and $N_D = 1.29$. Fig. 3a

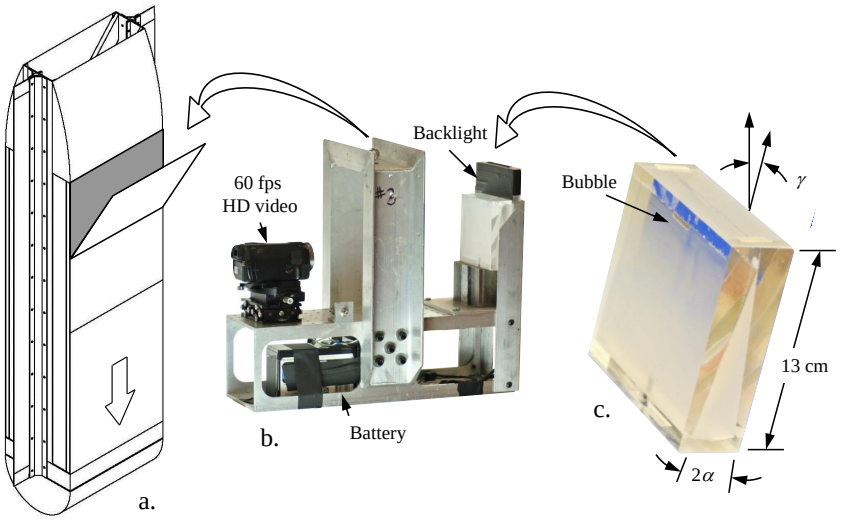

Figure 2. Drop tower test equipment: a. free-falling drag shield that houses b. the experiment rig that supports c. the sealed inverted wedge test channel of acute vertex half-angle $\alpha = 7.75°$ at tilt angle γ.

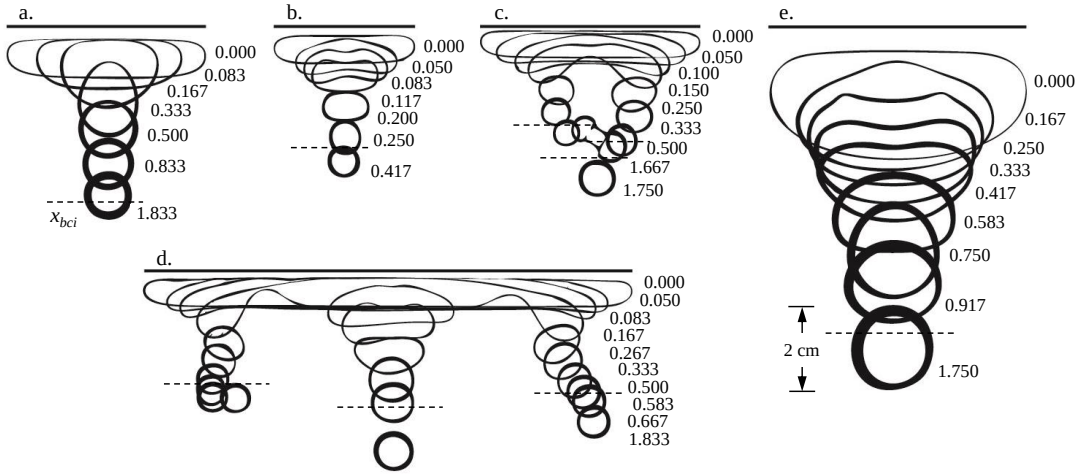

Figure 3. Downward capillary bubble migration in drop tower tests depicted in Fig. 2: a. bubble volume $V_b = 0.093$ ml, fluid 10 cs PDMS (drop test number 2313), b. 0.029 ml, fluid HFE-7500 (3168), c. 0.041, HFE-7500 (2326), d. 0.099, HFE-7500 (2317), and e. 0.495, HFE-7500 (3180). All images are shown to the scale shown in e. and for times listed next to each projected profile. All tests are performed for $\gamma = 0°$ except e. where $\gamma = 82°$. Projected bubble center ideal inscribed locations x_{bci} are identified using dashed lines.

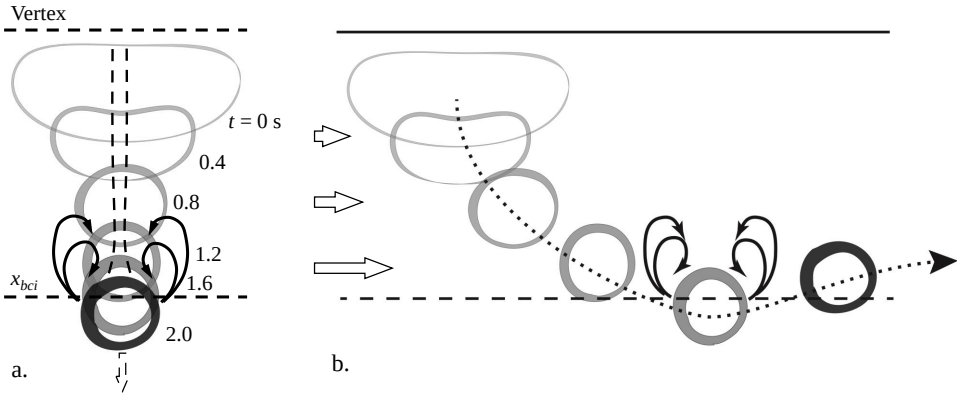

Figure 4. Depictions of wake vortices for small-to-intermediate inertial capillary bubble migrations: a. Drop tower test of $V_b = 0.495$ ml HFE-7500 fluid with $Q_l = 0$ ml/s and $\gamma = 82°$ with flow pattern identified from particle seeding. The bubble is still moving at $t = 2$ s. b. Conceptual superposition of field in a. and non-zero base flow with intermediate Q_l. The inscribed bubble center elevation x_{bci} is sketched as a dashed line.

provides a viscous example more in line with the experiments performed by [10]. The more inertial flow in Fig. 3b reveals early stage opposing corner flows that create a small geyser distorting the bubble enroute to its spherical configuration. The initially larger, longer bubble of Fig. 3c distorts significantly to the point of break-up. In this example, the fissioned bubbles re-merge migrating further away from the vertex toward the new inscribed elevation. However, re-mergers do not always occur as shown in Fig. 3d. Tilting the test cell, as noted by γ in Fig. 2c, allows much larger single bubbles to be studied without break-up. Such a test is shown in Fig. 3e, where $\gamma = 82°$. Following a step reduction in gravity, the interior corner flows are again observed to wick across the vertex where they collide forming a geyser. The distorted bubble avoids the breakup observed in 3c, but the highly inertial capillary flow displaces the oscillating non-circular projection of the bubble well away from the vertex. A sequence of overlayed images from a similar drop tower experiment employing a particle seeded liquid is shown in Fig. 4a where wake vortices are obvious as also observed by [10]. Inertia in the recirculating fluid is sufficient to carry the bubble past the ideal inscribed elevation x_{bci} beyond which capillary forces no longer provide a motive force. For the end state images shown for each test in Fig. 3, in 3a the over-damped bubble is creeping toward its ideal spherical inscribed elevation x_{bci}. In 3b the bubble is slowly circulating clockwise in the left eddy (ref. Fig. 4). In 3c and 3e all bubbles are still moving past their ideal inscribed elevations, but in 3d the bubbles appear to be caught in their own wake vortices which act to reverse their motion back in the direction of the vertex and the inscribed location x_{bci}.

Considering only tests with appreciable inertia, Fig. 5a provides projected bubble centroid histories for the drop tower tests of Figs. 3b and e with select data from [10]

and a selection of CCF EU2 experiments performed on ISS, the latter with convective flow rate set to the minimum value of 0.5 ml/s, as will be described shortly. The relevant properties and dimensions of the tests in Fig. 5 are listed in Table 1. The time coordinate of Fig. 5a is scaled by $(\rho/\sigma)^{1/2}$ in 5b which achieves a useful linear collapse and not as observed by [12]

$$x_c \approx 0.335 \left(\frac{2\sigma}{\rho V_b^{1/3} \alpha^{2/3}} \right)^{1/2} t, \tag{3}$$

with ρ the density difference across the interface–approximately equal to the liquid density. But the linear region of the Fig. 5b curves appear independent of bubble volume V_b and wedge half-angle α as expressed in eq. 3.

Much is yet to be learned. For example, inertial bubble migration is further complicated when an inertial convective liquid base state is present as investigated herein. Coupling the capillary bubble migration flow field with the base flow field produces a variety of outcomes that are not adequately understood. Low volume bubbles achieve essentially low inscribed elevations in regions within the base flow boundary layer where path lines are over-damped. Larger inertial bubbles are driven beyond their inscribed elevations where free stream-like developing base flow velocities displace them downstream in such a manner that they are entrained in their own recirculating wakes and driven back toward the vertex and their inscribed elevations. This general behavior is depicted in Figs. 1 and 4b for a base flow. Fig. 1 adds the presence of a free surface. We note that such bubble motion reversals are also readily observed in quiescent host liquids due to slight flow geometry asymmetries; i.e., Fig. 3d. As will be seen, and as identified by [12], the overshoot phenomena is less pronounced as the liquid flow rate is increased. But questions remain concerning bubble elevations in such developing shear flows. For example, do the bubbles drift away from inscribed elevations? Are they forced into slightly confined elevations? Or both ([2])?

The details of such phenomena are important to the design of large length scale bubble separation processes and capillary fluidic devices aboard spacecraft. They are also ideally studied aboard spacecraft. Related microgravity experiments have been performed aboard the International Space Station (ISS), but have focused on imbibing bubbly capillary flows with flow velocities that are intrinsically tied to irregular and often tapering polygonal conduit geometry (i.e., [14], [15], and [16]). As the large bubbles are displaced across the containers due to corner wicking flows, smaller bubbles convect into narrow bubble bypass regions where they are in turn confined and coalesce with the free surfaces of the larger bubbles. In this way such constructs serve the function of passive phase separation. But in such experiments, both liquid and gas flows are coupled and capillarity-driven. In reference to the flow geometry of Fig. 1, the ability to drive the liquid flow independently of the gas flow enables a wide range of test conditions. Employing a pump and an open wedge channel of variable length, the Capillary Channel Flow experiments (CCF) are conducted aboard the International Space Station (ISS) to collect a large unearthly data set to inspire advanced capillary fluidics design as well as guide further fundamental and applied research. The implications to terrestrial applications and

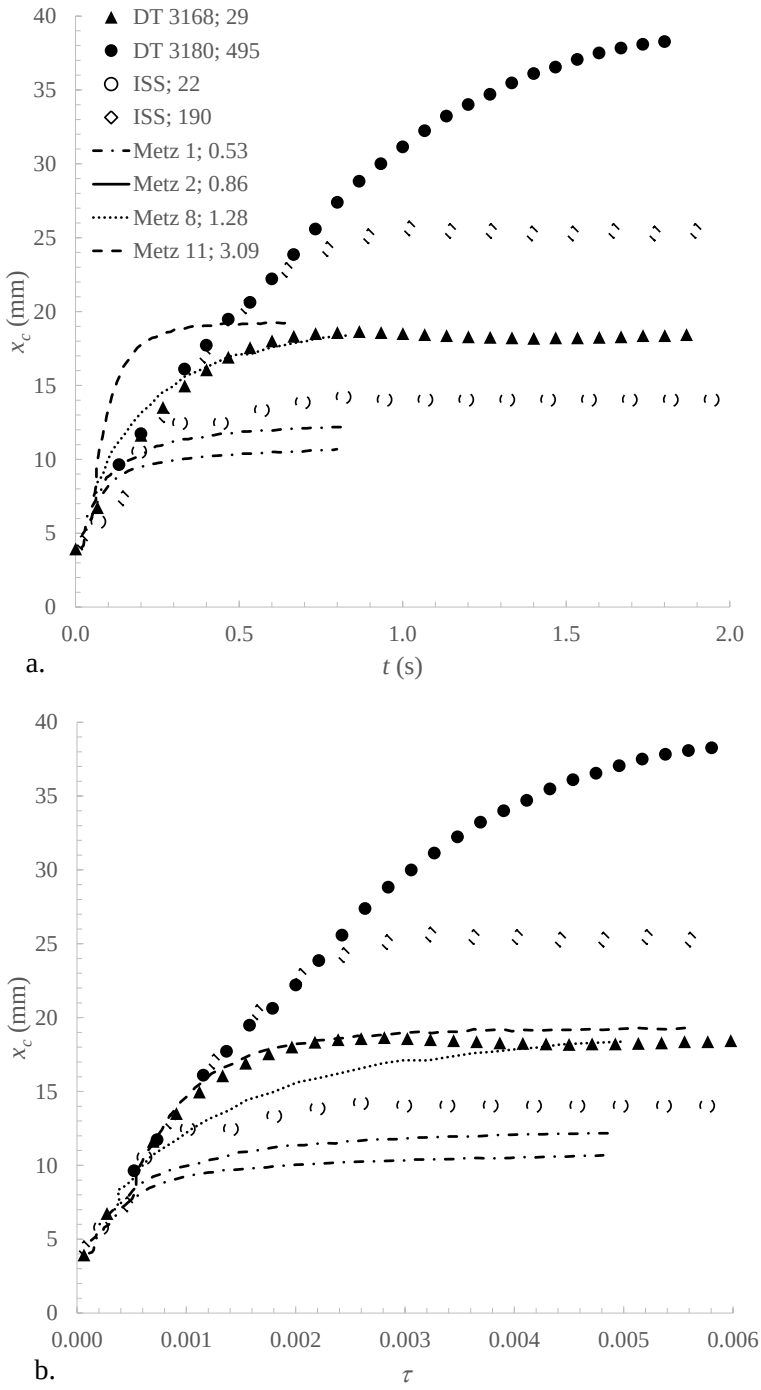

Figure 5. a. Projected bubble center location x_{bc} for a variety of predominately inertial bubble migration tests for bubble volumes listed in μl: drop tower (DT), ISS, and selected tests from [10]. For the drop tower tests refer to Fig. 3b and e, respectively. The data of a. is re-plotted with $\tau \equiv t(\sigma/\rho)^{1/2}$. The apparent linear region of the collapse suggests bubble volume-independent behavior. Refer to Table 1 for specific properties and test conditions.

Table 1. Fluid properties and test cell dimensions for test data in Fig. 5. Metz et al. [10] employ a 120 g/l concentration of aqueous isopropyl alcohol. $Su^+ \equiv (\rho\sigma V_b^{1/3}/\mu^2)\tan^{8/3}\alpha$ is viewed as a measure of inertia in an otherwise visco-capillary flow [12].

Source	Fluid	Test #	V_b (μl)	σ (N/m)	ρ (kg/m^3)	μ (kg/m·s)	θ (deg.)	α (deg.)	Su^+
DT	HFE-7500	3168	29	0.0162	1614	0.00124	0	7.75	268
DT	HFE-7500	2326	41	0.0162	1614	0.00124	0	7.75	301
DT	HFE-7500	2317	99	0.0162	1614	0.00124	0	7.75	404
DT	HFE-7500	3180	495	0.0162	1614	0.00124	0	7.75	691
ISS	HFE-7500	-	22	0.0162	1614	0.00124	0	7.9	264
ISS	HFE-7500	-	190	0.0162	1614	0.00124	0	7.9	536
Metz	Isopropyl	1	0.53	0.035	967	0.0017	9	2.75	2.9
Metz	Isopropyl	2	0.863	0.035	967	0.0017	9	2.75	3.4
Metz	Isopropyl	8	1.28	0.035	967	0.0017	9	2.0	1.7
Metz	water	11	3.09	0.072	1000	0.001	9	2.75	32.2

the overlap with terrestrial research are also important aspects of the work.

2 Regime Map Definitions, and Nomenclature

As a means of introducing most of the definitions and nomenclature for this work, in Fig. 6 we provide a sketch of a generic fixed bubble frequency flow regime map for a narrow open wedge channel similar to that sketched in Fig. 1. For fixed channel geometry, injected bubble frequency f, and fluid properties including a perfectly wetting liquid, each map will be presented in terms of the gas Q_g and liquid Q_l volumetric flow rates. The gas flow rate is controlled by varying the bubble volume V_b such that $Q_g = fV_b$. As in related investigations (see [17] and many references contained therein), the magnitude and ratio of Q_g and Q_l determines the particular regime. Flow conditions outside of these regimes are unsustainable in terms of time-averaged steady liquid flow. At least 6 regimes and 3 regime boundaries are identified in Fig. 6. Each is named from the perspective of such channels serving as low-gravity passive bubble phase separation devices. A selection of representative images for each regime and regime boundary described is provided in Fig. 7. Corresponding definitions and descriptions are provided as follows:

1. 0% Singles: All single bubbles with 0% separation. In other words, the relatively small bubbles do not reach the free surface. We call this the 0% separation condition where all bubbles convect through the exit of the open wedge channel.

2. Partial Singles: All single bubbles with partial separation. For the fixed length channel, and for a variety of reasons, at least one of at least ten of these relatively intermediate-sized bubbles reach the free surface, coalesce, and leave the flow. Only a portion of the bubbles convect through the channel exit.

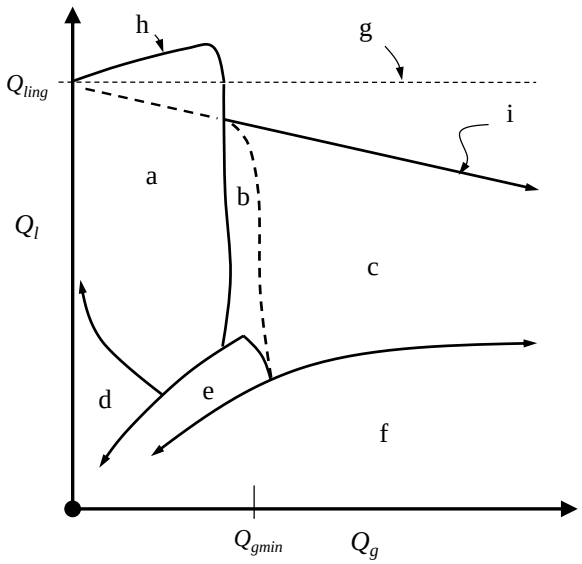

Figure 6. Sketch of a generic fixed-bubble frequency regime map in an open wedge channel: a. 0% separated single bubbles, b. partial singles, c. 100% singles, d. 0% mergers, e. partial mergers, f. 100% mergers. The single phase ingestion limit Q_{ling} (choking) is identified by the dashed horizontal line g. The map is bounded above by a region of bubble enhanced free surface stability h. and free surface bubble coalescence enhanced ingestion i. (Refer to text for definitions and to Fig. 7 for images of the various regimes.)

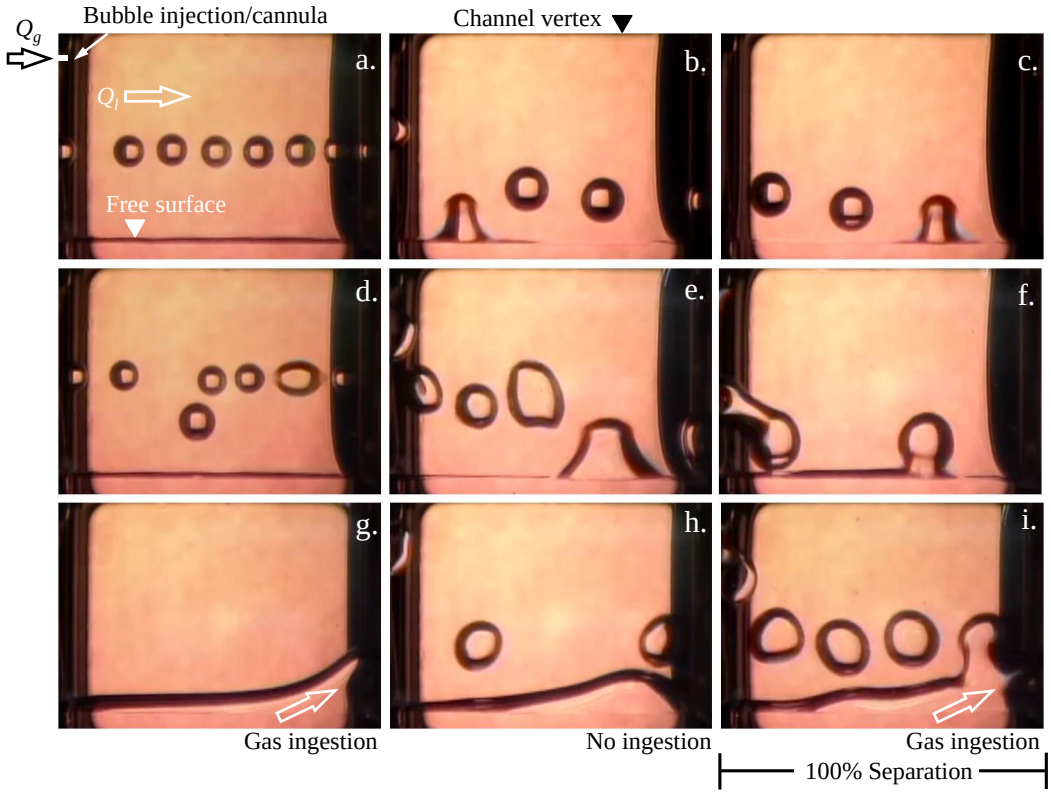

Figure 7. Characteristic images corresponding to the generic fixed-bubble frequency regime map in an open wedge channel from Fig. 6: a. 0% singles, b. partial singles, c. 100% singles, d. 0% mergers, e. partial mergers, f. 100% mergers, g. gas phase ingestion, h. bubble enhanced stability, and i. free surface bubble coalescence enhanced ingestion. Refer also to Fig. 1 for the approximate orientation on the conduit.

3. 100% Singles: All single bubbles with 100% separation. 100% of these relatively large single bubbles reach the free surface, coalesce, and leave the flow. No bubbles pass through the channel outlet.

4. 0% Mergers: At least one of at least ten bubbles merge with each other with 0% separation. The single bubbles may merge, and merged bubbles may merge, and so on, but the merged bubbles are still not large enough to reach the free surface for the fixed length channel. This is a 0% separation state since all single and merged bubbles convect through the channel exit.

5. Partial Mergers: At least a portion of the bubbles merge with partial separation. Single-, double-, triple-, and so on, mergers produce a variety of bubble volumes, a portion of which are large enough to reach the free surface, coalesce, and leave the flow. Only a portion of the single as well as merged bubbles convect through the channel exit. Here, 'mergers' defines bubble to bubble coalescence events, while 'coalescence' defines bubble to free surface coalescence events.

6. 100% Mergers: A 100% separation state where at least some bubbles are observed to merge. Merger rates generally decrease with increasing Q_g. No bubbles pass through the channel outlet.

7. Single Phase Ingestion Limit: Without any bubbles injected, for fixed channel dimensions, Q_l is limited by the stability of the free surface and values of $Q_l > Q_{ling}$ lead to collapse of the free surface near the channel exit and periodic ingestion of ambient gas bubbles into the liquid flow loop (choking).

8. Bubble Enhanced Stability: 0% single bubbles enhance the stability of the free surface and allow Q_l to achieve values above the ingestion limit Q_{ling}.

9. Coalescence Enhanced Ingestion: The advent of bubbles leaving the free surface results in an abrupt drop in the maximum value of Q_l possible for the flow. Partial single- and increasingly merged-bubbles, towards 100% separation at intermediate to high gas flow rates, continue to reduce the liquid depth and thus ingestion limit Q_{ling}.

The effect of wetting conditions on the regime maps is expected to be significant, [18]. We expect mergers to dominate behavior in interesting ways as $Q_l \to 0$.

A brief narrative of the space experiment, components, procedures, and calibration is provided before introducing the experimentally determined regime maps. Following some discussion, simple heuristic arguments are used for effective prediction of the regime boundaries.

3 CCF Story

The Capillary Channel Flow experiment (CCF) hardware was launched to the International Space Station (ISS) aboard the Space Shuttle Discovery (STS-131) on April 5th, 2010. For all subsequent operations, the equipment is installed by an astronaut

into the Microgravity Science Glovebox (MSG) facility of the Destiny Module of the ISS, [19]. Once installed, the MSG is sealed, the equipment is powered, and the experiment is commanded remotely and continuously from ground stations primarily at ZARM-Bremen and PSU-Portland, but also from Astrium-Friedrichshafen and NASA-MSFC as needed. The hardware includes three open test channel geometries: parallel plate, rectangular groove, and wedge channels. Beginning December 27, 2010, CCF was first operated 24 hours per day for 80 continuous days with the parallel plate and rectangular channels. The primary objective of these tests was to determine the critical liquid flow rates of such channels that mark the collapse of the free surface and the initiation of bubble ingestion—a condition often called choking by [20], and herein referred to as the ingestion limit Q_{ling} (refer to Fig. 7g). A description of these experiments, including a more thorough review of the experiment equipment and function, is provided in [21]. Future CCF ISS experiments with parallel plate and rectangular groove channels are scheduled.

The first operation of the wedge test channel experiments began on September 13, 2011 and continued for 33 24-hour days. The results of these initial tests are reported in part in [12]. These tests also identified the ingestion limits for this geometry, but included exploratory tests on bubble and bubbly flows in the wedge channel where the upstream gas flow boundary condition was that of a constant volume reservoir. In this series of tests, short bursts of bubbles were studied such that the upstream gas pressure did not decrease significantly during the injection, enabling the assumption of an essentially constant pressure gas reservoir condition. This approach was effective in defining a limited variety of flow regimes as a function of gas flow rate, liquid flow rate, and bubble frequency, but not always the bubble volume, [12]. Conditions demarking the 100% passive bubble separation conditions were also identified. Much was learned during the first round of wedge channel tests not the least being the breadth of capabilities of the experiment hardware despite the numerable challenges presented when seeking to precisely control multi-phase systems in a reduced-gravity environment, [22]. For example, the CCF flight hardware incorporates a minimum of four, what might be called, passive phase separation devices in addition to the primary wedge test channel which was designed to study passive phase separation! Thus, there were many opportunities to destabilize the system, invert the fluid phases, and/or otherwise leak or spill away the liquid contents of the triply-contained system. Most fortunately, complete recovery following all purposeful or inadvertent destabilizations was possible through nearly continuous commanding of the experiment from the ground and sending over 200,000 commands to ISS for CCF at average rates exceeding one per minute with peaks of over five commands per minute.

A second operation of the wedge test channel experiments continued for 40 24-hour days beginning June 17, 2013. The ingestion limit investigations continued during these operations, but extensive bubble phase separation tests using new fixed bubble volume conditions were conducted. It is these specific tests that are the subject of this paper. The fixed bubble volume approach combined with ample-resolution real-time video downlink from the ISS provided a wealth of data that are highly complimentary to the previous 'constant upstream pressure' tests of [12]. A brief review of the CCF hardware is followed by system calibration data used to

'parachute' into the desired experimental conditions and determine the uncertainty limits of the measurements. Over 5,000 data points were collected for a variety of conditions and these are presented here primarily in the form of regime maps. The many regime transitions are discussed in light of simple idealized models that describe much of the complex behaviours observed. Further insights are learned from subsets of the data that quantify velocity fields, bubble coalescence lengths, bubble merger transients, and more. The paper is concluded with a description of the continued directions of the work highlighting the immediate application of the results towards passive phase separations in low-gravity environments, as well as in microfluidics systems on earth. The unique, approximately 1TB dataset and video log including image rectification algorithms, recommended instructions for use, etc. is made publicly available following a request for access at http://psi.nasa.gov.

4 CCF Flow Loop Overview

A highly simplified schematic of only the pertinent components of the CCF flow loop is presented in Fig. 8. Referring to the figure, a self-priming external Micropump GB-P25 gear pump (a) is employed, which at low flow rates, pumps liquids and gases equivalently. Vane structures in the Phase Separation Chamber (b) reroute the HFE-7500 liquid around the coalesced Nitrogen gas bubbles and a screen serves as a bubble trap. Thus, only liquid passes through the Phase Separation Chamber (b) and into the Flow Preparation Chamber (c) where a converging duct delivers a highly laminar, though developing, flow to the Test Channel (d).

The pressure of the system is set by a 60 mm diameter meniscus in what is referred to as the Compensation Tube (e) connected to the Flow Preparation Chamber (c) upstream of the Test Unit (f). The transparent Compensation Tube (e) is open to the ambient gas environment of the Test Channel (d). The quartz Test Channel is a 15.8° open wedge 48 mm in length and 30 mm in height. A sliding lid allows variation of the free surface length $0.1 \leq L \leq 48$ mm within the field of view. The channel is backlit by a diffused incandescent source and the two Hitachi HV-C20 Series 640 px by 480 px color CCD camera fields of view are identified by the red dashed domains in Fig. 8. Bubbles are injected ≈ 2 mm upstream of the Test Channel inlet from a 223 mm long, 0.8 mm OD, 0.6 mm ID cannula (g) with centerline 3.6 mm from the channel vertex. The gas flow is driven by a gas plunger (h) delivering $0.0273 \leq Q_g \leq 273$ ml/s, which is regulated using a high speed Festo MHE2-MS1H-3/2O-M7-K solenoid valve (i) capable of a wide range of frequencies $0.01 \leq f \leq 10$ Hz and duty cycles $0.001 \leq d \leq 10$ s. Further geometric details of the flow path are conveyed in the half-section solid model of Fig. 9, including a more faithful depiction of the cannula configuration. The entrance region leading to the test channel is an elliptic contraction from the Flow Preparation Chamber. The exit contraction begins 19.5 mm downstream of the test section and consists of a rather abrupt transition to a 10.7 mm ID tube that is centered with respect to the Test Channel height at 15 mm.

During the tests, bubbles coalescing with and leaving through the free surface, at times, eject droplets that float or fly within the Test Unit until colliding, sometimes

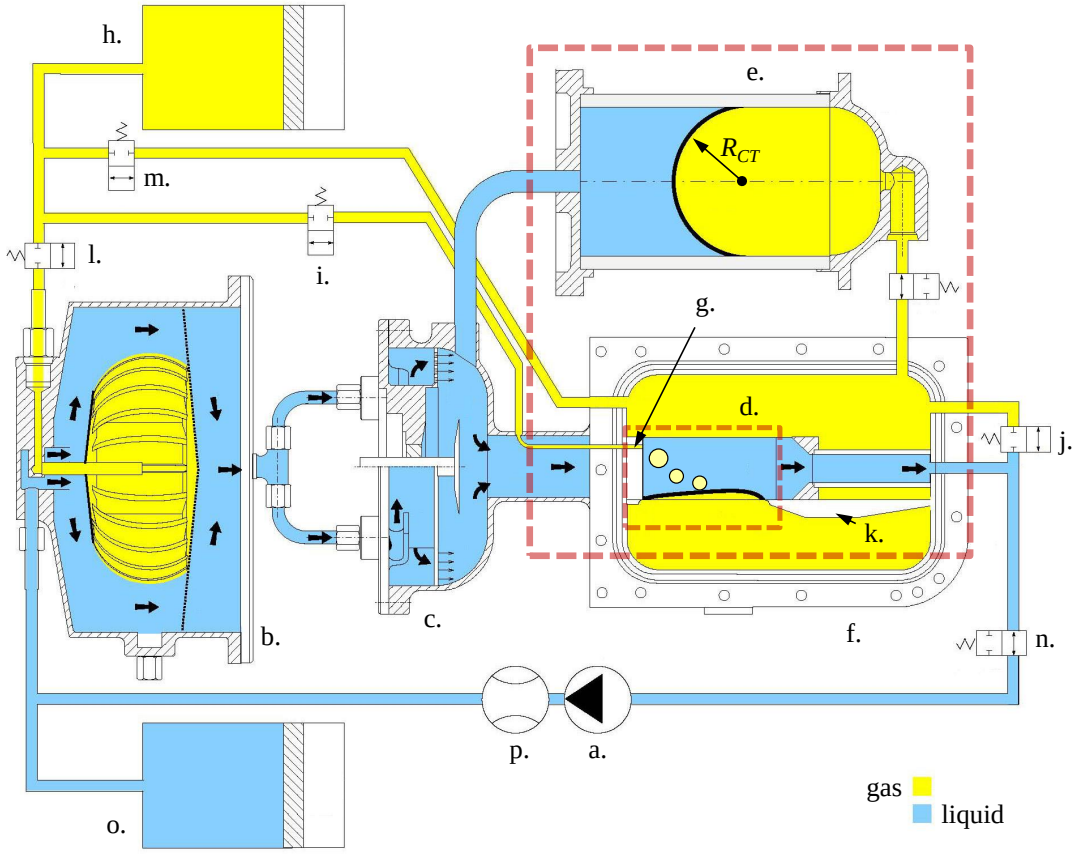

Figure 8. Schematic of primary plumbing elements for the CCF open wedge channel experiment (CCF EU2). The two camera fields of view are identified by the red dashed domains. As mentioned in order of the text the key items are a. the gear pump, b. Phase Separation Chamber, c. Flow Preparation Chamber, d. transparent Test Channel, e. transparent Compensation Tube, f. transparent Test Unit, g. notional cannula (ref. 9), h. N_2 gas reservoir and plunger, i. bubble valve (solenoid), j. liquid recovery port valve, and k. slider. Control valves l., m., and n., and HFE-7500 liquid reservoir and plunger o. are used to position the fluid phases, and p. is the flow meter.

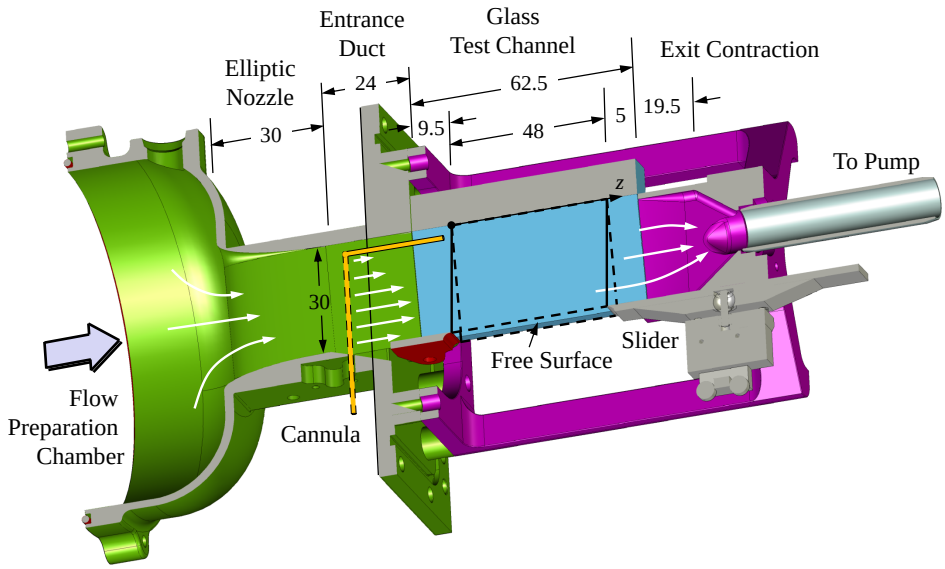

Figure 9. Half-section solid model of flow geometry into, through, and out of the Test Channel with critical entrance flow lengths noted (cf. Fig. 8). The viewable region of the Test Channel is outlined in black: 48 mm long, 30 mm high, and of half angle $\alpha = 7.9°$. Notional velocity fields are sketched in white.

rebounding, and ultimately adhering to the Test Unit interior walls. Such 'splashing' in addition to ingestions and other interface destabilizations lead to capillary connections outside the Test Channel that leak liquid away by capillarity. These splash and leak rates were measured and found negligible compared to the pump flow rates Q_{pump} for the tests conducted. However, over time these liquid losses accumulate large amounts of liquid in the Test Unit. Fortunately, this liquid could be recovered by either drawing the liquid through a Liquid Recovery Port (j), or by closing the slider (k) and running the pump at a high flow rate such that an under-pressure in the Test Channel returned the liquid by suction via an unbroken capillary connection past the slider surfaces and to the liquid throughout the Test Unit. These liquid recovery methods would almost certainly not have worked if the liquid was not perfectly wetting. Other valves (l)(m)(n) are employed along with a liquid reservoir and plunger (o) to re-position the fluid phases between tests.

A custom Electrical Ground Support Equipment (EGSE) interface is tailored for telemetry with NASA's Telescience Resource Kit (TReK). Exactly 494 discrete states are monitored at 1 Hz, 82 of which are directly manipulable by the experiment operator team. Only 36 of the states are critical to this report and include system temperatures, pressures, valve states, flow rates, fluid levels, etc. Key control parameters include pump flow rate Q_{pump}, gas plunger volume displacement rate $\dot{V}_1$ (ml/s), plunger volume V_1 (ml), slider position L (mm), bubble valve frequency f (Hz), and bubble valve duty cycle d (s). During each test, data is collected manually from the EGSE display and entered into spreadsheets, generating control curves

and guiding the data collection process and strategy. During the 640 hours required of these tests, 5,315 data points were collected requiring hundreds of thousands of keystroke entries. Accompanying the data are individual GMT time-stamped video recordings linked to the precise conditions of each test.

Both data and video logs are made publicly available at http://psi.nasa.gov. Suggestions concerning the structure and use of the archive are presented in part in Appendix A. Upon completion of the experiment operations, the telemetry logs are extracted from the TReK databases to correct typographical, transcription, and omissions errors that occurred during the manual collection of data. The majority of the data collected is presented here in the form of regime maps for either fixed bubble frequency or fixed bubble volume conditions. These approaches are all enabled by the ability to deliver known bubble volumes at desired frequencies, as confirmed by in-flight calibrations to ensure this capability.

5 Calibration Experiments

5.1 Cannula ΔP and Bubble Volume V_b

To quickly establish injected bubbles of known volume in a closed loop system, a quasi-steady pressure difference across the Bubble Valve and cannula $\Delta P \equiv P_1 - P_2$ needed to be rapidly achieved using *a priori* target values for gas flow rate $Q_g \equiv fV_b \approx \dot{V}_1(1 + \Delta P/P_2)$, where f and V_b are the bubble frequency and volume, the quantity $\dot{V}_1$ is the gas plunger displacement rate in ml/s, and P_1 and P_2 in mBar are the effective upstream and downstream pressures across the cannula. Referring to Fig. 8, P_1 is measured in the gas line just downstream of the gas reservoir h and P_2 is measured in the Flow Preparation Chamber c just upstream of the test channel. A zeroth order approach assumes a steady process where the gas within the cannula is compressible, viscous, and fully-developed such that

$$\Delta P \approx \frac{8\pi\mu l_c}{A_c^2}\frac{\dot{V}_1(1 + \Delta P/P_2)}{fd} \approx 12.47\frac{\dot{V}_1(1 + \Delta P/P_2)}{fd}, \tag{4}$$

where $l_c = 223$ mm is the cannula length, $A_c = 0.283$ mm^2 is the cannula cross sectional area, and $\mu = 18 \cdot 10^{-6}$ kg/m·s is the dynamic viscosity of the N_2 gas at 29.4 ± 0.6°C, which are substituted and evaluated in the right hand form of eq. 4. The experimental data serves the double purpose of system calibration and a best fit using eq. 4 yields

$$\frac{\Delta P}{1 + \Delta P/P_2} \approx 16.62\frac{\dot{V}_1}{fd}, \tag{5}$$

where the coefficient 16.62 (mBar· s/ml) accounts for additional viscous resistance in the Bubble Valve and other gas supply plumbing (compare with the theoretical coefficient 12.47 in eq. 4). Eq. 5 is presented in Fig. 10a against experimental measurements. For the range of parameters tested ($0.04 \le f \le 8$ Hz, $0.0035 \le d \le 5$ s, $0.0273 \le \dot{V}_1 \le 1.1466$ ml/s, and $1093 \le P_2 \le 1190$ mBar where $P_2 \approx 1128.8 \pm 13.3$ mBar), average uncertainties for the prediction of ΔP are less than $\pm 10\%$ and usually less than $\pm 5\%$ in the primary test range of $20 \le \Delta P/(1 + \Delta P/P_2) \le 30$

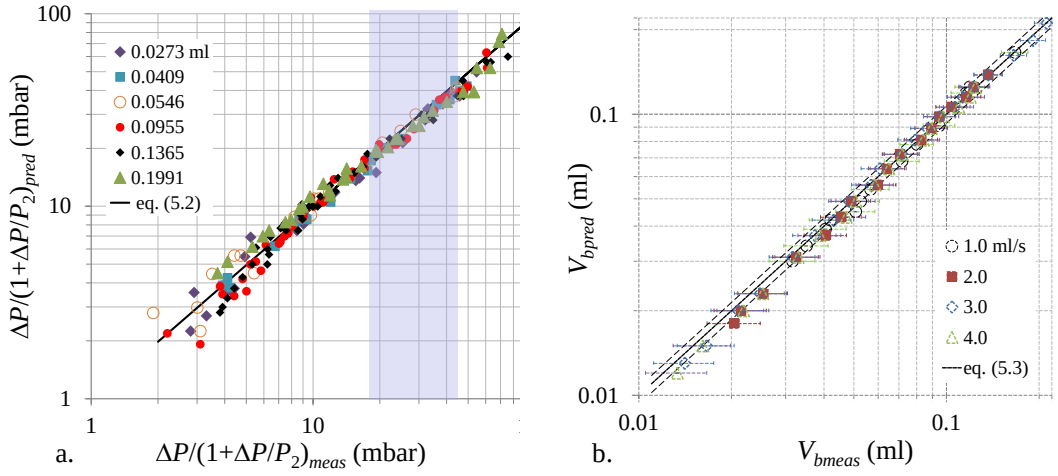

Figure 10. Predicted vs. measured results for a. ΔP as a function of bubble volume V_b (ml) and b. injected bubble volume V_b as a function of liquid flow rate Q_l (ml/s). The shaded region in a. identifies conditions for the wide majority of the tests conducted and the $\pm 7\%$ uncertainty is identified in b.

mBar, where typically $20 \leq \Delta P \leq 30$ mBar with standard deviations of prediction uncertainties ± 1.3 mBar. Thus, on average $P_1 \approx 1129 + 25 \approx 1154$ mBar.

With knowledge of ΔP, bubble volumes may then be estimated using

$$V_b \approx \frac{\dot{V}_1}{f}\left(1 + \frac{\Delta P}{P_2}\right), \tag{6}$$

and for experimental values $0.004 \leq V_b \leq 2.14$ ml, values for $0.027 \leq Q_g \leq 1.179$ ml/s are achieved for the tests conducted. Bubble volume measurements are non-linearly dependent on the image resolution of bubble diameter measurements, the latter of which are at worst $\pm 4\%$ for the smallest bubbles and at best $\pm 1.5\%$ for the largest bubbles. Thus, the uncertainty for the smallest bubble volume is less than $\pm 12\%$ while that for the largest bubble bubble is less than $\pm 5\%$. Uncertainty of bubble volume determines the uncertainty of the gas flow rate, and indirectly, the liquid flow rate in situations where gas bubbles leave the Test Channel exit as will be discussed. The results of calibration experiments comparing measured spherical bubble volumes to predictions using eq. 6 are shown in Fig. 10b. A fit coefficient in eq. 6 is once again expected to correct for un-modelled effects such as added resistances in the bubble valve, but we find here that none is needed for bubble volume predictions within typically $\pm 7\%$, as identified in Fig. 10b. Thus, measured Q_g uncertainties are on average $\lesssim \pm 7\%$. Eqs. 5 and 6 are used to *predict* the test conditions required to construct the regime maps that will be presented shortly; the latter which employ the subsequently *measured* conditions.

For a higher order accounting of the transients and compressibility in the gas delivery system, the compressible viscous flow model applied to Fig. 11 is used to

derive the governing dimensionless nonlinear transient first order ODE for pressures $P_1^* = P_1/P_{1i}$ and $P_2^* = P_2/P_{1i}$, where

$$(1-\beta t^*)\frac{dP_1^*}{dt^*} + P_1^{*2}\left(1-\phi^2\left(1-\beta t^*\right)^2\right) - P_1^*\left(\beta - 2\phi(\Omega+\phi)\left(1-\beta t^*\right)\right) = (\Omega+\phi)^2, \tag{7}$$

subject to $P_1^*(0) = 1$, and

$$P_2^* = \Omega + \phi - \phi P_1^*\left(1-\beta t^*\right). \tag{8}$$

$P_2^*(0) = P_{2i}/P_{1i} \equiv \Omega$ is the initial pressure ratio, $\phi = V_{1i}/V_2$ is the initial gas volume ratio, and $\beta = 2\dot{V}_1/\bar{c}P_{1i}$ is the dimensionless upstream plunger volume displacement rate, where $V_1(0) \equiv V_{1i}$ is the initial known gas plunger volume, $\dot{V}_1$ is the steady gas plunger rate (this time in m^3/s), and $\bar{c} = A_c^2/(1.25)8\pi\mu l_c$ is a cannula viscous resistance parameter in $\mathrm{m}^4{\cdot}\mathrm{s}/\mathrm{kg}$, where the correction coefficient 1.25 accounts for bubble valve and line losses. This model extends that employed by [12] for a constant V_1 gas delivery approach which is recovered from eq. 8 when $\beta = 0$ ($\dot{V}_1 = 0$). Here, the dimensionless time employed is $t^* = \bar{c}P_{1i}t/2V_{1i}$, where $t \leq V_{1i}/\dot{V}_1$ is time in seconds (ref. to Fig. 11 for notation). With knowledge of P_1^* and P_2^* from eqs. 7 and 8, the *dimensional* quasi-steady gas flow rate may be determined using

$$Q_g = \bar{c}P_{1i}\left(\frac{P_1^{*2} - P_2^{*2}}{2P_2^*}\right). \tag{9}$$

For the wide majority of the experimental conditions $109 \leq V_{1i} \leq 247$ ml and $V_2 \approx 1108 \pm 76$ ml; V_2 is essentially equal to the sum of the average gas volumes in the Test Unit ($716 \leq V_{gTU} \leq 816$ ml), the Phase Separation Chamber ($115 \leq V_{gPSC} \leq 239$ ml), and the Compensation Tube ($124 \leq V_{gCT} \leq 206$ ml). Thus, in general, $\phi \lesssim 0.2$, $\beta \ll 1$, and $\Omega \approx 0.987$. In the vicinity of this parameter space, eqs. 7-9 are solved and presented in Fig. 12 for $\beta = 0$, 0.003, 0.031, and 0.05. Trends of both initially decreasing or increasing P_1 are observed, and though constant pressures are never achieved, these experiments seek states where $P_1^* - P_2^*$ approaches a steady value, producing a nearly steady non-zero value for Q_g. Such is only possible for $\beta > 0$. This capability is the significant difference between the current experiments and those of [12] where $\beta = 0$ and experiments were performed over short durations for $t^* \ll 1$ in hopes of limited decreases in $Q_g/\bar{c}P_{1i}$ during each test.

With further regard for the present $\beta > 0$ approach, locally steady flow rates are observed as $\beta t^* \to 1$. Taking $\beta t^* = 1$, eqs. 7 and 8 reduce to

$$P_1^* = \frac{\beta}{2} + (\Omega+\phi)\left(1 + \frac{\beta^2}{4(\Omega+\phi)^2}\right)^{1/2}, \tag{10}$$

and

$$P_2^* = \Omega + \phi, \tag{11}$$

respectively. Eq. 9 becomes

$$Q_g = \frac{\beta\bar{c}P_{1i}}{2}\left(\left(1 + \frac{\beta^2}{4(\Omega+\phi)^2}\right)^{1/2} + \frac{\beta}{2(\Omega+\phi)}\right), \tag{12}$$

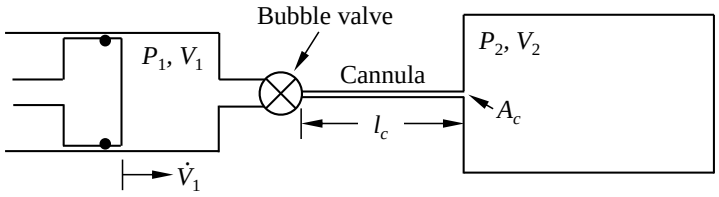

Figure 11. Simplified closed loop model of fully-developed isothermal ideal gas flow through a narrow cannula. The flow is driven by the upstream gas plunger.

which for $\beta^2/4(\Omega+\phi) \ll 1$ yields

$$Q_g \approx \frac{\beta \bar{c} P_{1i}}{2}\left(1+\frac{\beta}{2(\Omega+\phi)}\right). \tag{13}$$

Re-dimensionalizing the terms in eq. 13 noting that at zeroth order $\bar{c} \approx Q_g/\Delta P$ and $Q_g \approx \dot{V}_1$, eq. 13 reduces to

$$Q_g \approx f V_b \approx \dot{V}_1\left(1+\frac{\Delta P}{P_{2i}}\right), \tag{14}$$

which recovers the form of eq. 6 used to predict the test conditions and establish the control curves for the majority of the data collection operations, $\Delta P/P_{2i}$ providing a small correction to the expected $O(1)$ balance $Q_g \approx f V_b \approx \dot{V}_1$ (refer to Fig. 10).

5.2 Liquid Flow Rate Q_l

The schematic of Fig. 13 provides a further simplified view of the flow loop. During each run, the system contained within the dashed boundary in the figure is slightly pressurized as gas is injected into it. As shown in §5.1, this pressurization is limited by the ratio of the mass of gas injected during each test to the initial mass of gas in the large volume system V_2. In agreement with the foregoing analysis for the volume of gas downstream of the cannula V_2, considering the worst case of a 2.8% compression and average compressions of $\lesssim 0.1 \pm 0.04\%$ for all tests conducted, the gas phase within this dashed region may be effectively considered incompressible during each individual test. Following from this assumption, a volumetric flow rate balance may be applied to the Test Channel, where at steady state $Q_{in} = Q_{out}$.

The controlled volumetric flow rates are the gas injection rate $Q_g \equiv Q_{gin} = f V_b$ and the pump flow rate Q_{pump}. Referring to Fig. 7, by counting single and/or merged bubbles, review of the video data readily yields values for the rate of gas leaving the Test Channel through the free surface Q_{gsout} and through the channel exit Q_{gout}. When bubbles are injected into the flow, the pressure increases in the primary circulation loop sketched in Fig. 13 and a portion of liquid leaving the Phase Separation Chamber is diverted to the slightly lower but constant pressure Compensation Tube. This rate is denoted by Q_{lCT}. At steady state the Phase Separation Chamber collects all gas entering it but passes only liquid, Q_{lpump}. Thus,

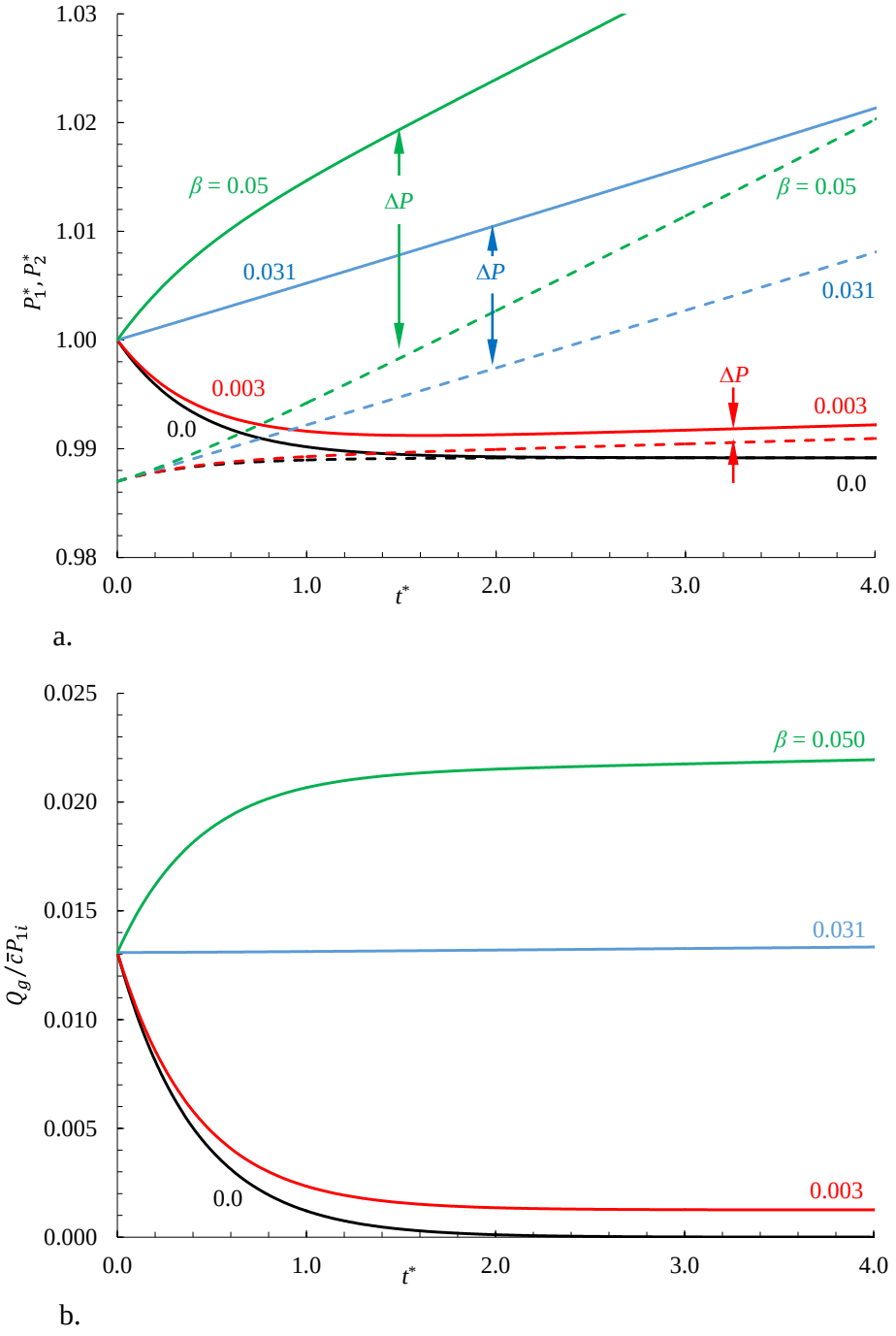

Figure 12. Numerical solution to eqs. 7–9 for a. P_1^*, P_2^*, and b. $Q_g/\bar{c}P_{1i}$: $\phi = 0.2$, $\Omega = 0.987$, and $\beta = 0$, 0.003, 0.031, and 0.05. Q_g is approximately constant as $\beta t^* \to 1$.

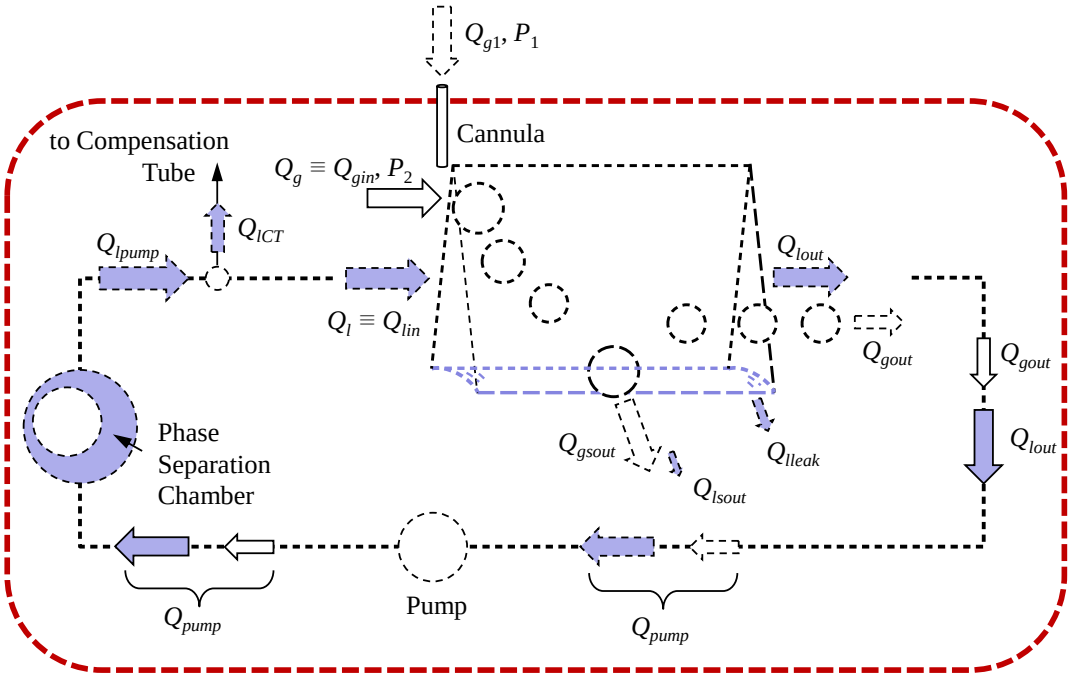

Figure 13. Simplified schematic of gas and liquid volumetric flows. Gas and liquid flow into the channel (Q_{gin}, Q_{lin}). Gas leaves the channel through the free surface and/or channel exit (Q_{gsout}, Q_{gout}). Liquid leaves the channel by splashing and leaking at the free surface as well as by convecting through the channel exit (Q_{lsout}, Q_{lleak}, Q_{lout}). The pump pumps both gas and liquid equivalently. The Phase Separation Chamber traps gas and passes liquid. A portion of the liquid flow is diverted to the Compensation Tube (Q_{lCT}). Neglecting Q_{lsout} and Q_{lleak}, one finds that $Q_{gout} = Q_{lCT}$ and $Q_{lin} = Q_{pump} - Q_{gout}$.

noting that $Q_{pump} = Q_{lout} + Q_{gout} \equiv Q_{lpump}$, and that $Q_l \equiv Q_{lin} = Q_{lpump} - Q_{lCT}$, balancing the volumetric flow rates into the channel with those leaving yields

$$Q_{gin} + Q_{pump} - Q_{lCT} = Q_{gout} + Q_{lout} + Q_{gsout} + Q_{lsout} + Q_{lleak}, \qquad (15)$$

where Q_{lsout} represents liquid leaving the channel through the free surface via droplet ejections (splash) during coalescence with the free surface, and Q_{lleak} is the ever-present and aforementioned capillary liquid leak rate from the channel. Specific tests conducted to determine the latter reveal that including a worst case 1:12 probability of droplet ejection during bubble-free surface coalescence, a worst case 1.5 mm diameter droplet, and a worst case frequency of 2 hz, $Q_{lsout} \lesssim 0.0038$ ml/s, which is 1% of the lowest flow rate of 0.38 ml/s employed in the experiments. By measuring the long duration decrease of the liquid level in the Compensation Tube, in the absence of bubbles with a fully open slider $L = 48$ mm, the liquid leak rate could be correlated with Q_{pump} to find $Q_{lleak} \approx 0.0099 - 0.0024 Q_{pump}$ (ml/s). This linearized relationship suggests that $Q_{lleak} = 0$ when $Q_{pump} \approx 4.08$ ml/s, suggesting further that the channel is continuously leaking for all tests, albeit at varying rates, since $Q_{pump} < 4.08$ ml/s for the wide majority of tests conducted. This correlation also implies that for values of $Q_{pump} > 4.08$ ml/s the leak rate takes negative values implying suction of liquid from outside the Test Channel back into loop, as described earlier as a method employed to recover leaked liquid to the flow loop. For the range of flow rates $0.38 \leq Q_l \leq 3.0$ ml/s it is found that $0.009 \geq Q_{lleak} \geq 0.003$ ml/s which confines the leak rate between 0.1% and 1.8% of Q_l for all tests conducted. Thus, by neglecting Q_{lsout} and Q_{lleak} and by applying $Q_{pump} = Q_{lout} + Q_{gout}$ and $Q_{gsout} = Q_{gin} - Q_{gout}$, eq. 15 reduces to

$$Q_{lCT} \approx Q_{gsout}. \qquad (16)$$

It is then found that

$$Q_l \equiv Q_{lin} \approx Q_{pump} - Q_{gout}, \qquad (17)$$

which is used to determine the liquid flow rates into the test channel since both quantities on the right hand side are readily measured. For the majority of tests performed at or above the 100% separation condition $Q_{gout} = 0$ and the liquid inflow rate is equal to the pump flow rate, $Q_l = Q_{pump}$. The quantitative results of [12] were largely restricted to this 100% separation condition.

The pump flow rate Q_{pump} is calibrated in-flight using the flow meter accurate to ± 0.1 ml/s to find the liquid flow rate $Q_l = 0.987 Q_{pump} - 0.11$ ml/s . Thus, Q_l uncertainties are expected to be as high as $\pm 25\%$ for the lowest flow rates of 0.38 ml/s, but $\lesssim \pm 4\%$ for flow rates at and above 3 ml/s. As a result, the lowest accuracy flow rate measurements arise for low Q_l and the highest values of Q_g where the single or merged bubbles do not leave through coalescence with the free surface (0% separation states). But uncertainties in Q_g contribute little under these restrictive conditions and Q_l uncertainties are expected to peak at $\pm 21\%$ at the lowest Q_l, while average uncertainties in Q_l are calculated to be $\pm 7\%$. Recall that Q_g average uncertainties are also coincidentally $\pm 7\%$, with worst cases of $\pm 12\%$ for the lowest gas flow rates and less than $\pm 5\%$ for the highest. Thus, the flow rate measurement accuracy increases with increasing flow rate and $\pm 7\%$ serves as a nominal estimate for the majority of data presented herein.

5.3 Image Processing

All images are rectified during image analysis to correct for slight camera rotation and skew lingering from the manual alignment of the optic elements by the astronaut during set-up. The rectification algorithm and instructions for use are included with the data archive at http://psi.nasa.gov. Absolute accuracy is better than 0.5 mm with approximately 0.112 mm/px resolution.

5.4 Data Reduction: Bubble Velocity Profile

Full CFD computations of developing forced single phase liquid flow through the wedge channel are conducted by [23], but computations accounting for the presence of highly deformable inertial bubbles are incomplete. Particularly for larger bubbles, the liquid flow field is highly perturbed often by their inertial capillary cross flow trajectories. Specific calibration tests are presented here to determine the velocity field using the bubbles themselves; in effect determining the 'bubble velocity profile' of the wedge flow geometry without resolving smaller scale structures such as wakes, eddies, waves, and disturbances to boundary layers, though all of these are observed.

In general, the various video events are further digitized to determine statistical transient free surface profiles and bubble cross sections, volumes, positions, and velocities. Sample video frames at 3 Hz of single bubble trajectories are overlayed in Fig. 14 for 10 bubbles of increasing volume at fixed flow rate $Q_l = 1.86$ ml/s and fully open slider, $L = 48$ mm. The frames are selected that assure the alignment shown at right in the figure where the wedge section is sketched to scale identifying the degree to which the bubbles are or are not inscribed within the channel. These flows are labeled as 0% singles and from eq. 17, $Q_l \approx Q_{pump} - fV_b$. As identified in Fig. 14, the positions of the bubbles are readily tracked by digitizing the locations of their rightmost edge x_b, which closely approximates both the projected area centroid and the halfway point between minimum and maximum x-coordinate elevations of the bubble surface x_{bc}. This is because the bubbles move downstream along nearly inscribed paths and are thus nearly spherical. For example, the leading edge bubble position data for the tests of Fig. 14 are presented in Fig. 15 with bubble volumes noted. Comparing x_b elevations at $z = 35$ mm with ideally inscribed elevations listed reveals that for these data the bubbles take inscribed or higher elevations.

For the case of Fig. 15, the blue data suggest viscous (over-damped) boundary layer behaviour for small bubbles near the wedge vertex ($V_b \lesssim 0.049$ ml) and the red data inertial (under-damped) free stream-like behaviour nearer to the free surface as bubbles increase in size ($V_b > 0.072$ ml). Values in yellow $0.049 \lesssim V_b \lesssim 0.072$ ml appear to be transitional, breaking the otherwise monotonic relationship between increasing bubble elevation x_b with bubble volume V_b.

As computed by [23], the velocity field experiences an abrupt change at $z = 0$ at the free surface where the no slip condition is replaced by the zero shear stress condition. With knowledge of this fact, fully-developed flow entrance lengths L_e are estimated assuming only free surface (FS) or only fully enclosed conduits (EC) to find

$$L_{eFS} \sim \frac{\alpha \rho Q_l}{\mu} \qquad \text{and} \qquad L_{eEC} \sim \frac{\alpha \rho Q_l}{\mu(1+\alpha)^2}. \tag{18}$$

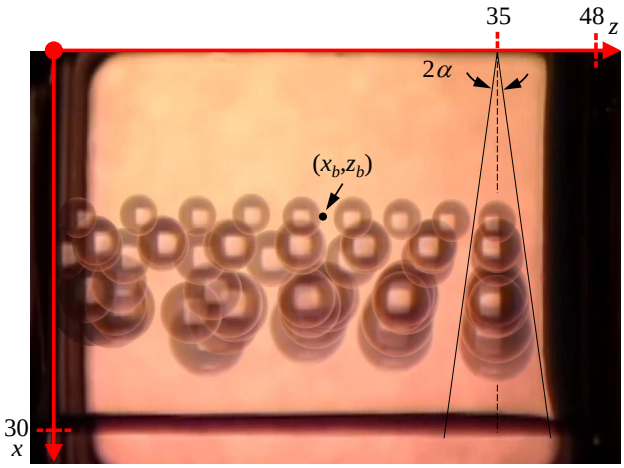

Figure 14. Image overlays of single bubbles tracked at 3 Hz intervals for bubble volumes identified in Fig. 15 for $Q_l = 1.86$ ml/s and $L = 48$ mm. At right is drawn the $\alpha = 7.9°$ wedge section to aid in visualizing the degree to which the bubbles inscribe at the $z = 35$ mm location. x_b identifies the rightmost edge of the bubbles tracked for elevation comparisons.

Referring to Fig. 9 the channel length from the inlet nozzle to the viewable channel exit is $30 + 24 + 9.5 + 48 = 63.5 + 48 = 111.5$ mm. From eq. 18, for the conditions of the present experiments, a fully developed base flow is expected only for $Q_l \lesssim 0.612$ ml/s for a free surface and $Q_l \lesssim 0.793$ ml/s for a fully enclosed channel (slider closed), respectively. Details for these forms are provided in Appendix C. The respective z-dependent fully-developed x-elevations for the two conditions in eq. 18 are approximated by

$$x_{eFS} \sim \left(\frac{\mu z_{ch} H^2}{\alpha \rho Q_l}\right)^{1/2} \qquad \text{and} \qquad x_{eEC} \sim (1+\alpha)\left(\frac{\mu z_{ch} H^2}{\alpha \rho Q_l}\right)^{1/2}, \quad (19)$$

where $z_{ch} \approx z + 63.5$ mm. The boundary layer elevation x_{eFS} is plotted against z in Fig. 15 establishing the approximate location of the developing boundary layer.

The ideal bubble center inscribed elevations x_{bci} with expected measurement uncertainties are shown at right in Fig. 15a. Though fully developed conditions are never achieved, discrepancies at $z = 35$ mm are blamed on the inertial capillary overshoot described in connection with Fig. 4 and the unique conditions where bubbles appear to interact with the edge of the boundary layer. The transitional bubble volumes $0.049 \lesssim V_b \lesssim 0.072$ appear most impacted, occupying elevations far higher than x_{bci}. Ten bubbles are used to determine the 10-point moving average fits shown in Fig. 15a. The repeatability of such data is high. For example, and for clarity, 10 sequential bubble paths for four bubble volumes $V_b = 0.018$, 0.043, 0.056, and 0.138 ml are shown in Fig. 15b. Even the transitional bubbles $V_b = 0.056$ ml take highly repeatable paths, but a bimodal behavior is observed in the case of $V_b = 0.043$ ml where 8 of 10 paths overlap while 2 of 10 diverge in the direction of

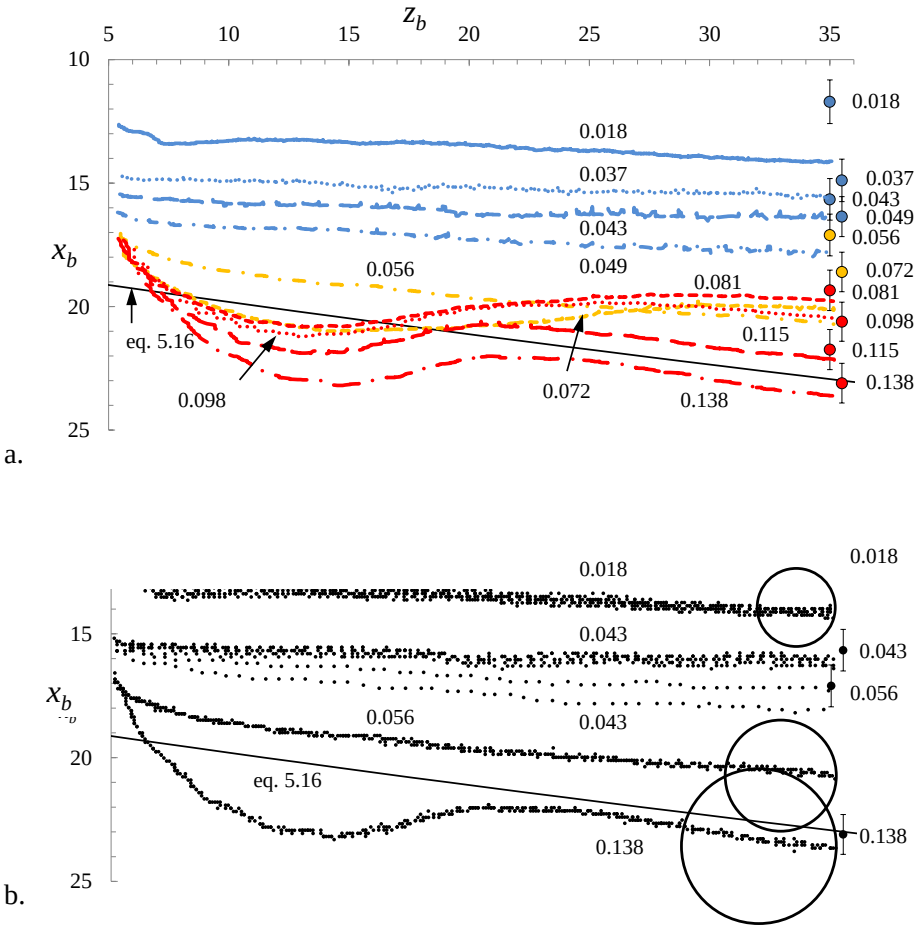

Figure 15. a. 10-point average bubble leading edge paths $x_b(t)$ for specified bubble volumes in ml with $Q_l = 1.86$ ml/s, $L = 48$ mm. Ideal inscribed bubble center elevations x_{bci} with uncertainties are shown at right. b. Bubble path data from a. of 10 consecutive bubbles for specified bubble volumes in ml. 2 of the 10 paths for $V_b = 0.043$ ml scatter. $x_{eFS}(z_{eFS})$ from eq. 19 is shown as solid line. Representative bubble diameters are sketched in b. for $V_b = 0.018$, 0.056, and 0.138 ml.

the boundary layer. Comparing Fig. 15b with the corresponding paths in Fig. 15a associates the degree of repeatability with the smoothness of the 10-point moving average fits shown in Fig. 15a.

Average z-coordinate bubble velocities $\langle w_b \rangle$ at the channel location $z = 35$ mm are presented in Fig. 16 using square symbols again for $Q_l = 1.86$ ml/s and $L = 48$ mm. The 'bubble velocity profile' is predominately linear within the boundary layer, but clearly loses this character beyond it as identified empirically by the dashed line and by eq. 19 identified by large + symbols and fitted with a smooth line, which suggest that the end of the linear behaviour is near the edge of the boundary layer. Idealized spherical bubbles are drawn at the terminus of the linear domains. The linear portions collapse such that $\langle w_b \rangle / Q_l \propto 1.205 \pm 0.067$ mm/ml (not shown).

The general trends of Fig. 15 arise despite the presence of the free surface and Figs. 17 and 18 repeat the results of Figs. 14 and 15, but for $Q_l = 2.85$ ml/s with the slider closed, $L = 0$ mm. At higher Q_l, x_b is often closer to x_{bci} accept for $V_b = 0.162$ ml which yield confined bubbles at $z = 35$ mm. Average bubble velocities for these conditions as well as other conditions for different slider locations are overlaid on Fig. 16 for further comparisons.

5.5 Discussion

From Figs. 15 and 18, in the boundary layer region of the flow a slight drift away from the vertex is observed to which local hydrodynamics may contribute such as Saffman lift, but such weakly non-parallel trajectories are observed from numerical simulations of the flow that show similar magnitude behavior due to local accelerations caused by the increasingly occluding free surface deflection and channel exit contraction effects, [23]. As suggested in Fig. 9, the exit contraction eventually drives all bubbles toward the exit tube elevation. An example full 3-D CFD simulation of the single phase liquid flow field provides a more quantitative picture in Fig. 19 (see [23] for further details). Thus, one might expect that nearer to the channel exit, small bubbles will be weakly driven away from the vertex and away from inscribed elevations, while large bubbles will be driven toward the channel vertex and toward or even past their fully inscribed elevations. Without further insights from theoretical and numeric analysis it is difficult to assess the magnitude of such effects though they are clearly less apparent with increasing Q_l as might be expected.

The simple flow visualization from drop tower tests shown in Fig. 4, and reported also by [12], reveal that for a quiescent liquid the inertial capillary bubble migration produces wake vortices that persist in carrying the bubble significantly past their inscribed elevations. When a base state liquid flow is present the liquid velocity profile convects the bubble downstream and increasingly away from these trailing wake vortices. As depicted in Fig. 4b, we currently conjecture that it is the recirculation of these vortices that results in the oscillatory nature of the intermediate-to-large bubbles at intermediate liquid flow rates. Such effects are less noticeable as Q_l increases (e.g., compare Fig. 15 with 18). It is also noted that at high bubble frequencies, subsequent bubble injections perturb previous bubble trajectories leading to further complexities of the flow.

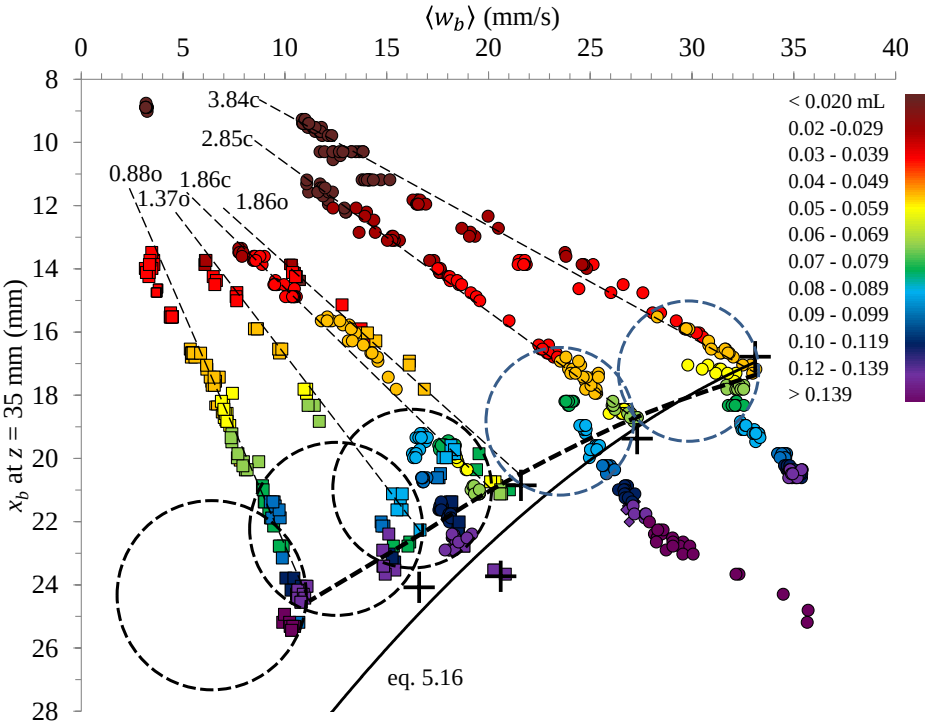

Figure 16. z-component bubble velocity $\langle w_b \rangle = fcn(x_b; V_b)$ at $z = 35$ mm. Flow rates and slider positions are identified for each data set where squares are for open slider conditions ($L = 48$ mm; i.e., $Q = 1.37o$ implies $Q_l = 1.37$ ml/s, slider open) and circles are for closed slider conditions ($L = 0$ mm; i.e., $Q = 2.85c$ implies $Q_l = 2.85$ ml/s, slider closed). Eq. 19 values are denoted by + symbols and fit with a smooth line as noted.

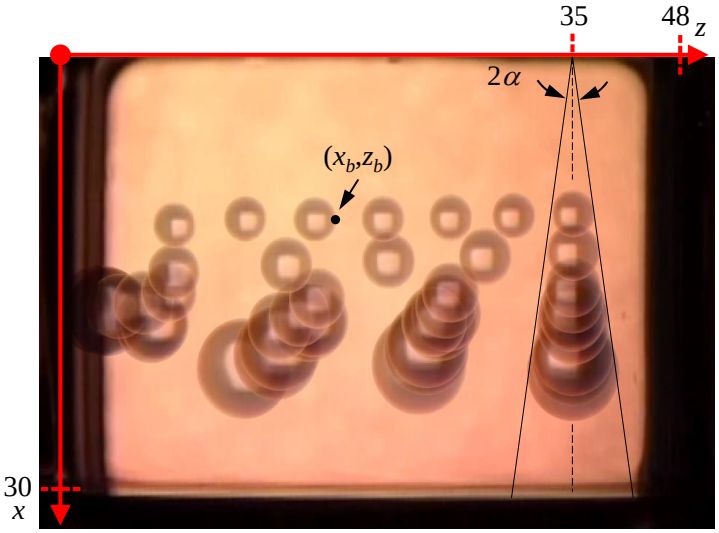

Figure 17. Image overlays of single bubbles tracked at 3 Hz intervals for bubble volumes identified in Fig. 18 for $Q_l = 2.85$ ml/s, $L = 0$ mm–no free surface. At right is drawn the wedge section to aid in visualizing the degree to which the bubbles inscribe at the $z = 35$ mm location.

5.6 Minimum Bubble Volume, V_{bmin}

From Figs. 14 and 17 it is clear that the elevation where the bubbles first become inscribed is central to the bubble behavior. For a fully developed parallel flow, whether or not the bubbles remain at inscribed elevations is dependent on the sign of the lift force in the asymmetric shearing flow. Both the direction and magnitude of these forces are yet to be learned. In fact, for our developing flow, according to [2] these forces may both change dramatically across the boundary layer. We do observe that for a flow rate of 2.85ml/s and closed slider the smaller bubbles in Fig. 18 take essentially parallel paths at essentially inscribed elevations. This might suggest a negative lift force if any. But we also observe in Fig. 15 for a flow rate of 1.86 ml/s and an open slider with a 48 mm long free surface that such bubbles migrate slightly away from the vertex – the smaller bubbles migrating away from inscribed elevations and the larger bubbles away from slightly confined elevations. This observation might suggest a potential combination of positive lift and capillary forces. However, we also acknowledge that the combined effects of the developing flow, free surface deflections, and the exit contraction contribute to non-parallel convective components, the degree of which is presently uncertain. Guidance from further theoretical and full CFD analyses is expected to clarify these issues.

With confirmation that the bubbles generally follow their inscribed trajectories, Fig. 20 provides a sketch of the wedge channel cross-section, liquid free surface, and minimum static inscribed spherical bubble volume that is tangent to the free surface. Values for key geometric quantities for these models are listed in Table 2. Though several model free surface configurations might be considered based

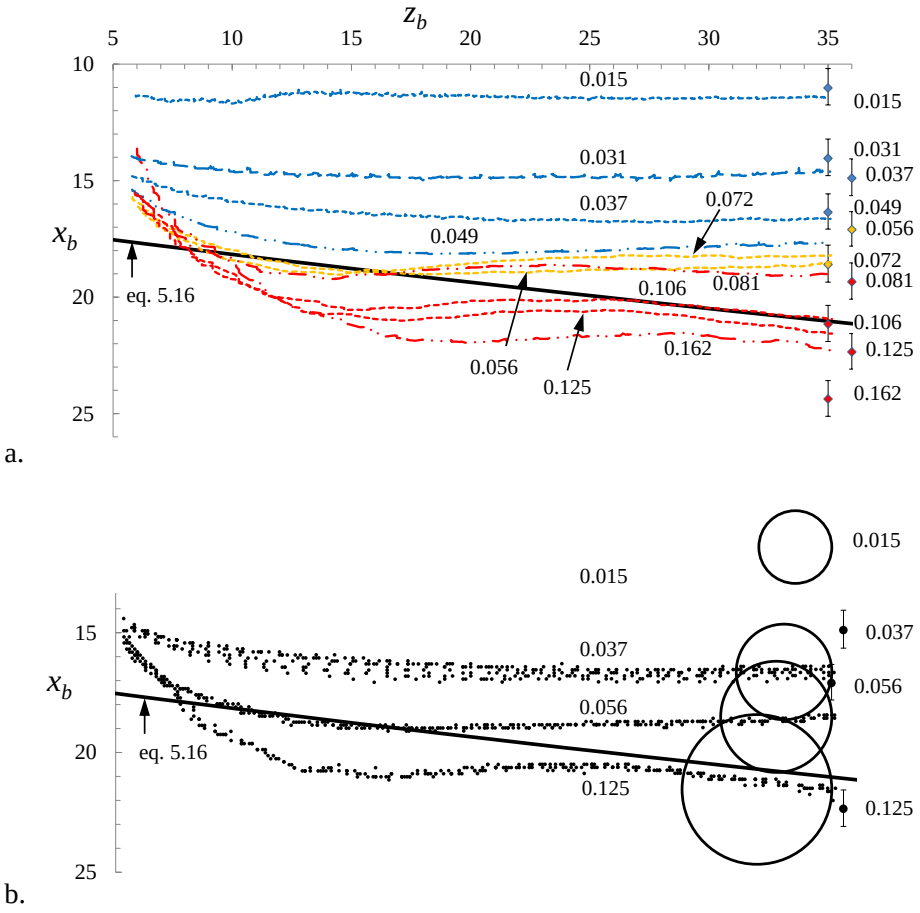

Figure 18. a. 10-point average bubble leading edge paths $x_b(t)$ for specified bubble volumes in ml with $Q_l = 2.85$ ml/s, $L = 0$ mm. Ideal inscribed bubble center elevations x_{bci} with uncertainties are shown at right. b. Bubble path data from a. of 10 consecutive bubbles for specified bubble volumes in ml. Most bubbles establish approximate inscribed elevations by $z = 35$ mm, with bubbles such a $V_b = 0.162$ ml clearly in confined elevations. $x_{eFS}(z_{eFS})$ from eq. 19 is shown as solid line. Representative bubble diameters are sketched in b.

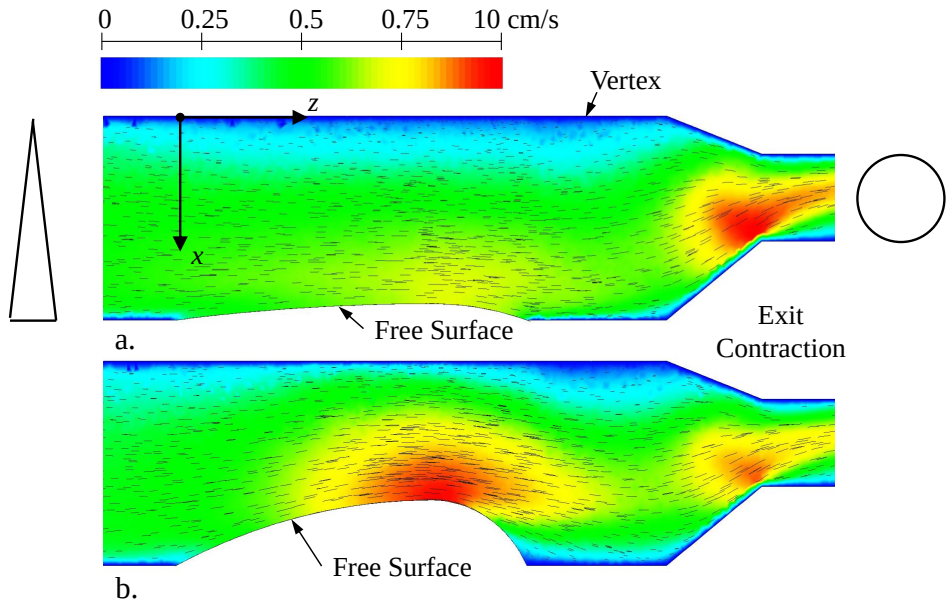

Figure 19. CFD velocity field predictions for a representative channel with representative fixed free surface profiles along center-plane with a. slight and b. significant free surface deflection to clarify the impact of free surface curvature and channel exit contraction on the non-parallel nature of the developing flow. The free surface is modelled as a rigid, zero shear stress surface where an elevated (normally super critical) flow rate of $Q_l = 5$ ml/s is achieved to amplify gradients. Note that the CCF exit port is centered at $x = 15$ mm and not shifted toward the vertex as computed here.

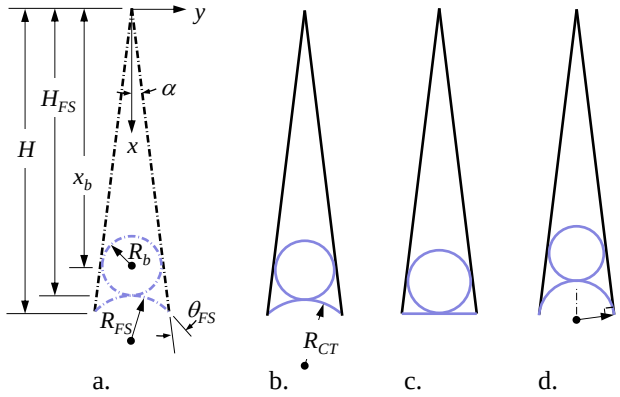

Figure 20. Models of minimum bubble volume V_{bmin} based on selection of tangential positions with the free surface: a. Arbitrary pinned free surface condition, b. no flow R_{CT} radius of curvature condition, c. flat interface, and d. tangent free surface. The flat surface model c. is selected as an easy guide for regime map predictions. Convex free surface models might also be considered. (Note that for a tangent bubble and free surface $H_{FS} = x_{bt}$.)

Table 2. V_{bmin} for the various models of Fig. 20: $\alpha = 7.9°$, $\theta_l = 0°$, $H = 30$ mm, $R_{CT} = 30$ mm. (Angles are expressed in radians unless otherwise specified.

Quantity	a. Arbitrary R_{FS}	b. $R_{FS} = R_{CT}$	c. $R_{FS} = \infty$	d. $\theta_{FS} = 0$
θ_{FS}	$\cos^{-1}(H\tan\alpha/R_{FS}) - \alpha$	74.1°	$\pi/2 - \alpha$	0°
H_{FS} (mm)	$R_{FS}(\cos\theta_{FS} - \sin\alpha)/\sin\alpha$	29.72	30.00	26.37
R_b (mm)	$H_{FS}\sin\alpha/(1+\sin\alpha)$	3.59	3.62	3.28
V_{bmin} (ml)	$4\pi R_b^3/3$	0.194	0.200	0.135

on arbitrary free surface curvature as in Fig. 20a, a flat surface approximation of Fig. 20c is simple, yields $V_{bmin} \equiv 0.20$ ml for the CCF experiments, and is essentially equivalent to the case of the Compensation Tube curvature in Fig. 20b, which more or less matches the Test Channel inlet pressure with radius of curvature $R_{CT} = 30$ mm. The minimum bubble volume that can reach the free surface with hopes of contacting, coalescing, and leaving the channel is selected to be $V_{bmin} \equiv 0.20$ ml. Obviously, and as reported by others, the value for V_{bmin} is foundational to the bubble separating characteristics of the wedge channel geometry.

6 Regime Maps

A wide variety of tests are conducted varying Q_{pump} (Q_l), f and V_b (Q_g), and slider length L. The majority of the results presented here are for fixed f and L, or for fixed V_b and L.

6.1 Fixed Bubble Frequency ($L = 48$ mm)

In Fig. 21 is presented the lowest complete bubble frequency regime map for $f = 0.2$ Hz ($L = 48$ mm). The data is also presented with expanded time coordinate in the inset. The symbols identify the various regimes using the definitions of §2 and are employed uniformly in all maps to follow. Figs. 22-27 present maps for $f = 0.5$, 0.75, 1, 1.25, 1.5, and 2 Hz using the same coordinate scale for ease of comparison. Approximate regime boundaries are sketched by eye on each map. The maps are combined in Fig. 28 with data and regime map boundaries provided in 28a and with regime boundaries and shaded regimes provided in 28b. Inspection of such maps elucidates several immediate conclusions. Other insights are drawn from inspection of the video data for each test condition. The observations listed here culminate in the generic map of Fig. 6 and correspond to the various fixed frequency regimes and regime boundaries associated with that figure in §2:

1. Low gas flow rates imply small gas bubbles that are too sparse to merge at elevated liquid flow rates Q_l. Single bubble volumes less than $V_{bmin} = 0.20$ ml cannot reach the free surface, coalesce, and separate.

2. Single bubbles with volumes slightly less or slightly greater than $V_{bmin} = 0.20$ ml on occasion reach the free surface, coalesce, and leave the flow. $Q_{gmin} = fV_{bmin}$ is identified in all maps where applicable. Bubble separations are enhanced due to the capillary overshoot depicted by the bubble position data exemplified in Figs. 4, 15, 18, and the inset of Fig. 21. A leftward hook in the vertical boundary between partial and 100% singles is observed near Q_{ling} due to increased free surface curvature. The severity of the 'hook' in these maps is muted compared to that of the different test conditions of [12].

3. Provided the channel is of sufficient length, single bubbles with $V_b > V_{bmin}$ ($Q_g > Q_{gmin}$) eventually reach the free surface, coalesce, and leave the flow.

4. At low Q_g small bubbles inscribe closer to the wedge vertex, well-within the boundary layer where the liquid flows are slower and mergers are enhanced. Merged bubble volumes $V_b < V_{bmin}$ cannot reach the free surface, coalesce, and separate.

5. Somewhat erratic mergers and multi-mergers lead to a distribution of bubble volumes, some of which exceed V_{bmin}, reach the free surface, coalesce, and leave the flow.

6. If $V_b > V_{bmin}/2$, mergers create bubbles of volume larger than V_{bmin}, and all such bubbles eventually reach the free surface, coalescence, and leave the flow. Thus, if Q_l is low enough the condition $Q_g = Q_{gmin}/2 = fV_{bmin}/2$ serves as a delimiter for 100% separating double-mergers. Mergers are enhanced for increasing frequency f, increasing bubble volume V_b, and decreasing liquid flow rate Q_l as easily observed in Fig. 28b.

7. The single phase liquid ingestion flow rate Q_{ling} approximately intersects the backwards-extrapolated terminus of the bubble coalescence enhanced ingestion boundary at $Q_g \approx 0$.

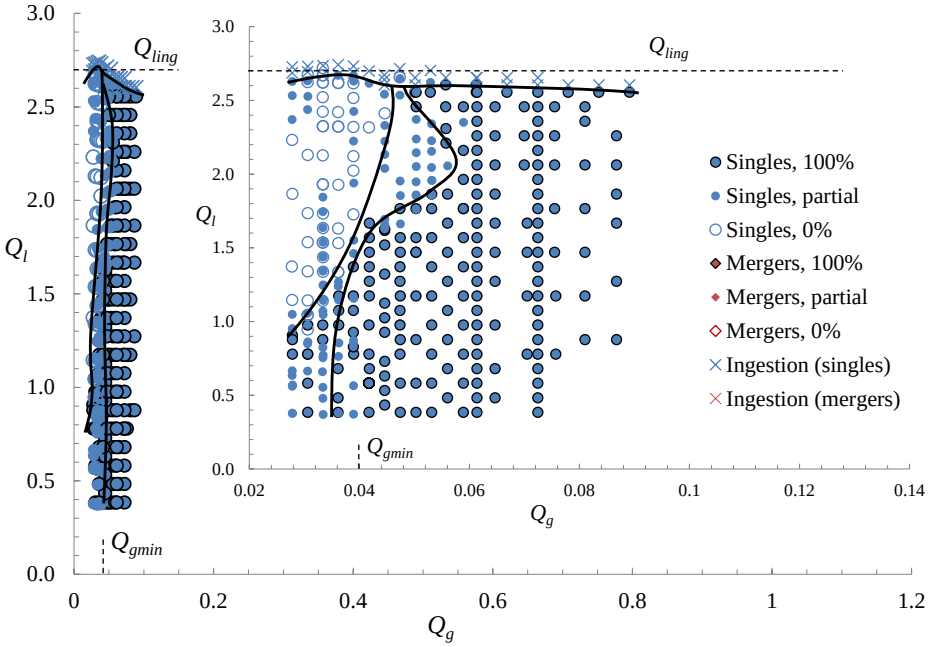

Figure 21. Regime map for bubble frequency $f = 0.2$ Hz with expanded scale inset.

8. At high Q_l, single bubbles of volume $V_b < V_{bmin}$ and frequency $f > f_{ing}$ stabilize the free surface and permit liquid flow rates slightly higher than the ingestion limit Q_{ling}. The stabilization is enhanced for increasing bubble frequency as observed Fig. 28b. To be reported separately, it is found that for channel lengths $L > 10$ mm, bubbles injected into the flow at frequencies higher than the gas ingestion frequency f_{ing} stave off the ingestion limit to flow rates as much as 2.2-fold the single phase flow ingestion limit, [24]. The source of this stabilization is still somewhat in question, but is likely attributable to the altered time-averaged boundary condition at the inlet which increases the system pressure, decreasing the free surface curvature, and increasing the flow cross section in the test channel allowing for higher flow rates with reduced viscous resistance. Note that f_{ing} is the frequency of gas bubble ingestion into the liquid stream at the channel exit at Q_{ling}.

9. At high Q_l, for $V_b > V_{bmin}$, single bubbles coalesce with the free surface reducing the local depth of the liquid and enhancing ingestion of ambient gas through the free surface at the channel exit. The slope of the bubble enhanced ingestion boundary is common to all fixed frequency maps.

6.2 Fixed Bubble Volume ($L = 48$ mm)

Each of the regime maps of Figs. 21-28 hold bubble frequency f constant and vary V_b and Q_l. In Figs. 29 and 30 two maps are presented where V_b is fixed and f

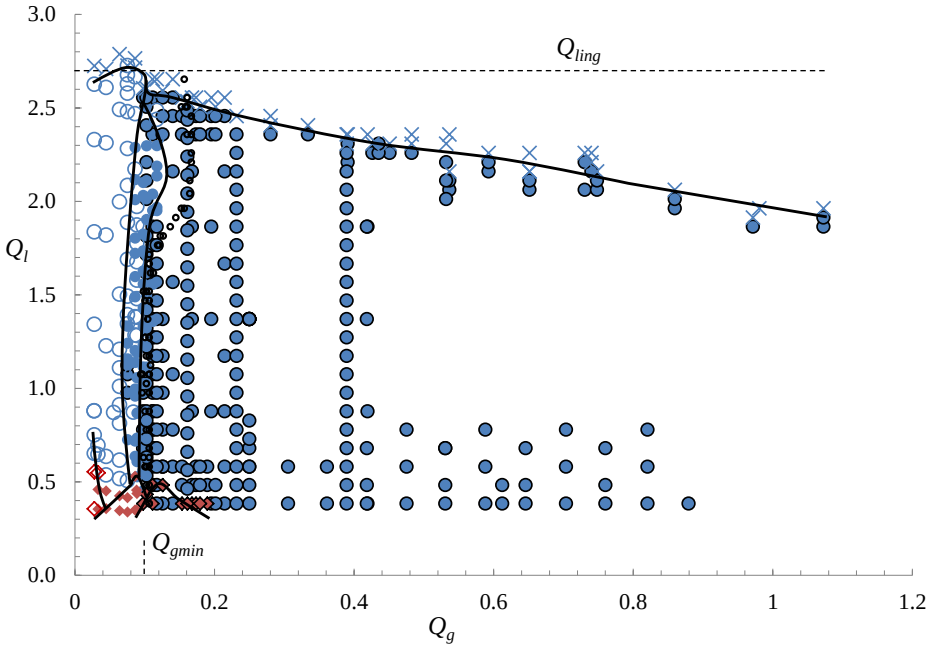

Figure 22. Regime map for bubble frequency $f = 0.5$ Hz. (Refer to Fig. 21 for symbols.) The small black open circles are taken from [12] as the 100% separation limit for the 'fixed volume' upstream condition of those experiments.

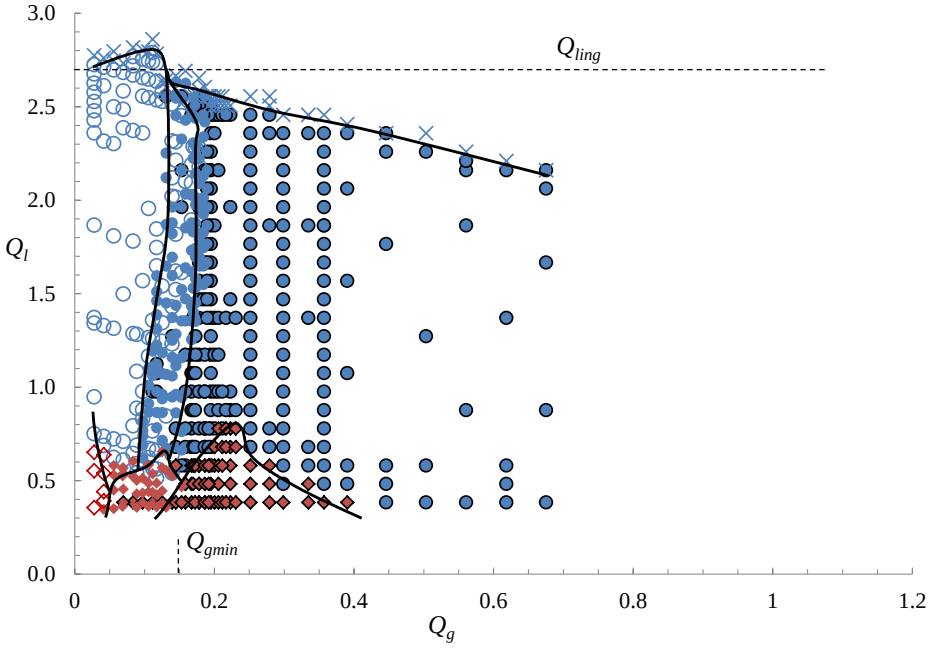

Figure 23. Regime map for bubble frequency $f = 0.75$ Hz.

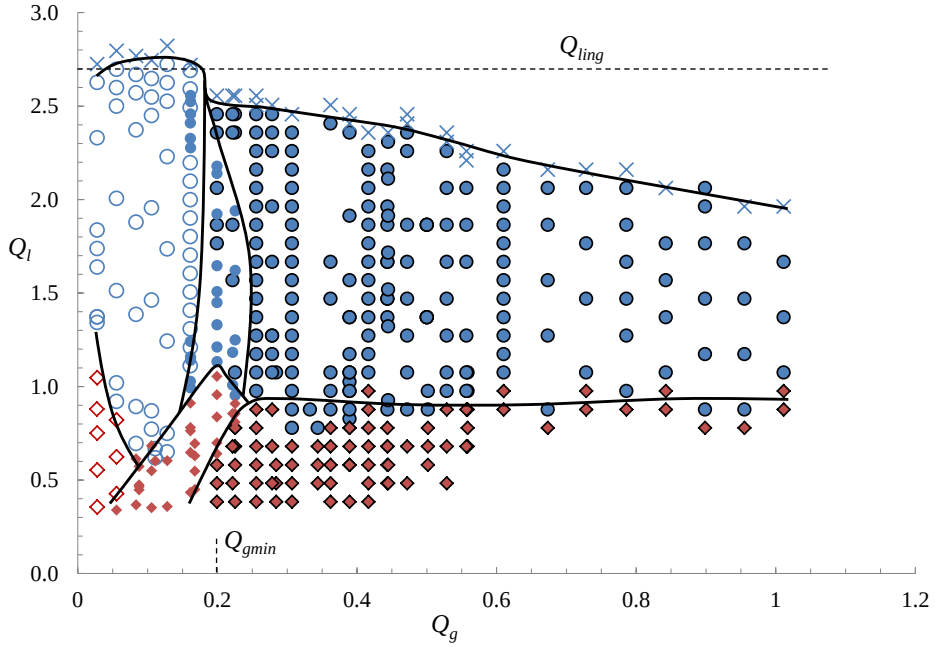

Figure 24. Regime map for bubble frequency $f = 1.0$ Hz.

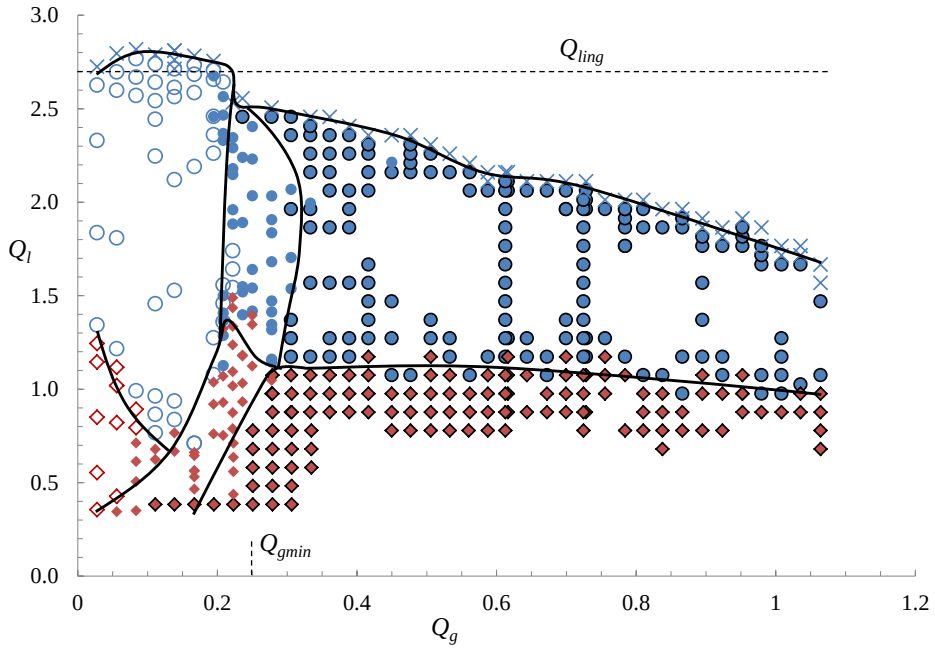

Figure 25. Regime map for bubble frequency $f = 1.25$ Hz.

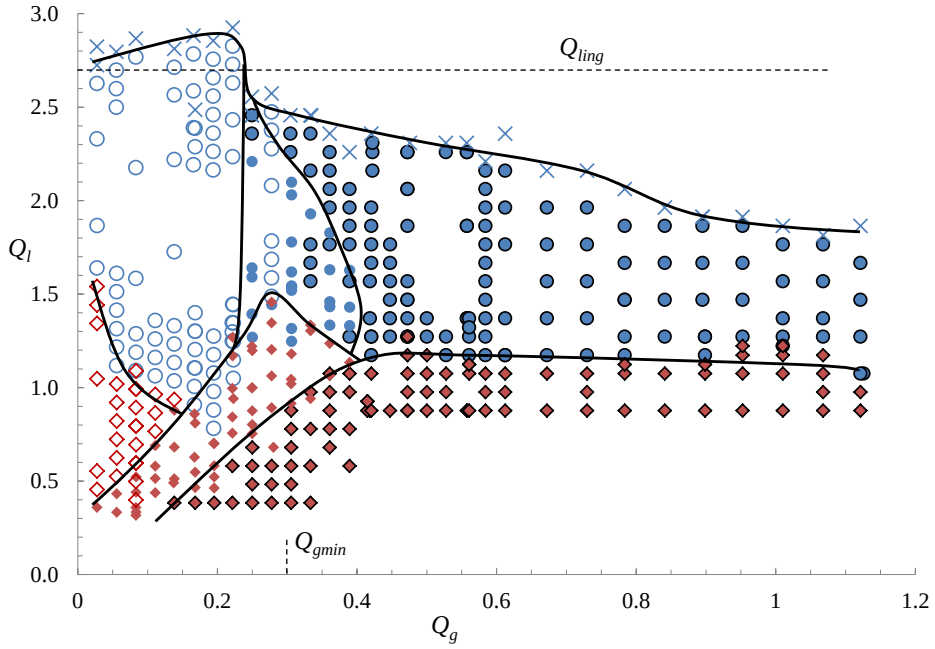

Figure 26. Regime map for bubble frequency $f = 1.5$ Hz.

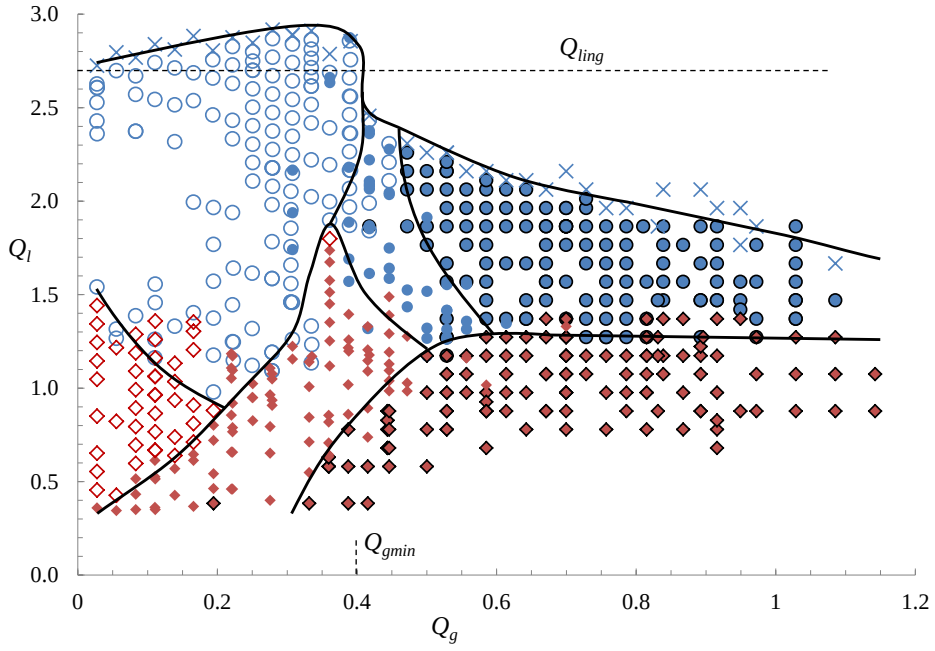

Figure 27. Regime map for bubble frequency $f = 2.0$ Hz.

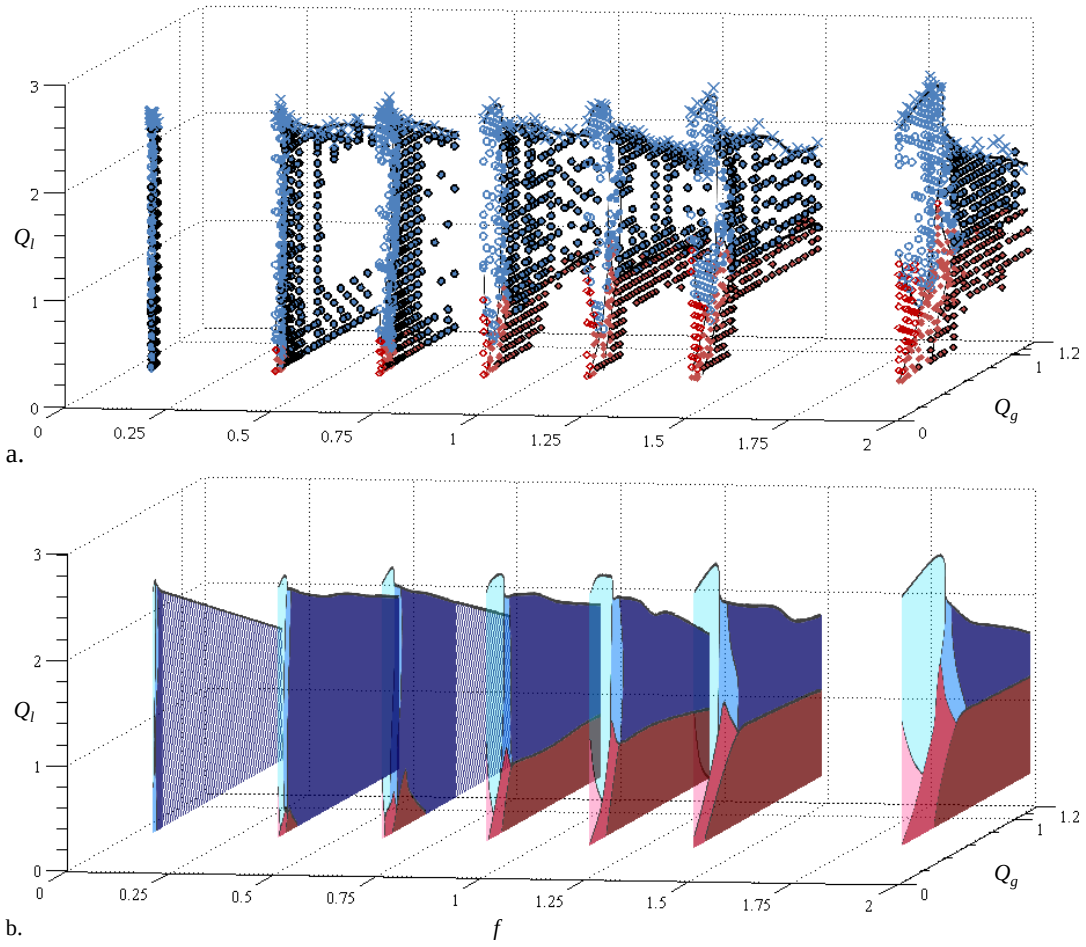

Figure 28. 3-D representation of regimes maps of Figs. 21-27, for $f = 0.2$, 0.5, 0.75, 1.0, 1.25, 1.5, and 2.0 Hz: a. data with regime boundary sketch, b. regime boundaries and shaded regimes. In b., for high Q_g, the 100% single bubble regime is extrapolated for $f = 0.2$ Hz and interpolated for $f = 0.75$ Hz.

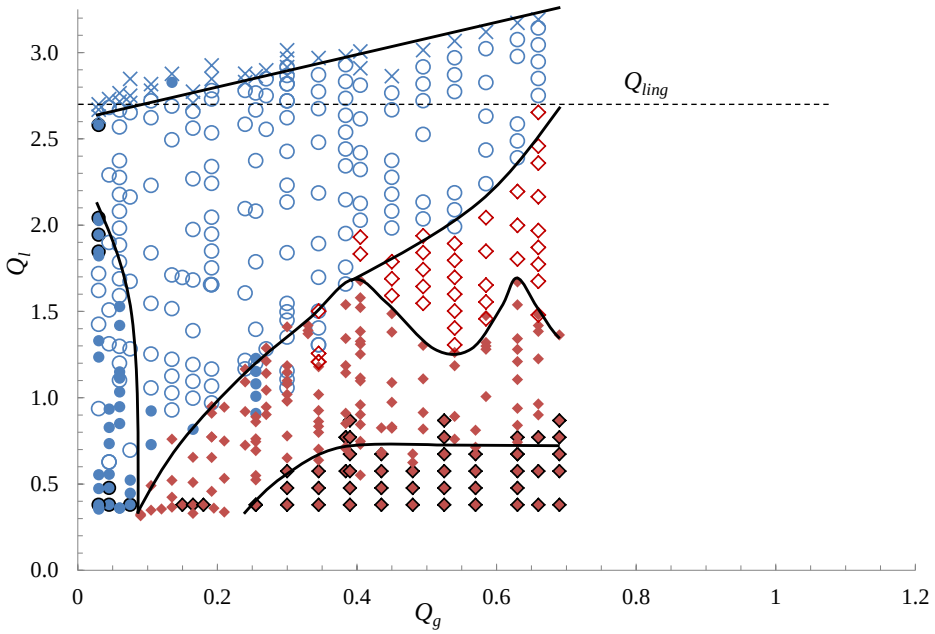

Figure 29. Regime map for fixed bubble volume $V_b = 0.15$ ml.

and Q_l are varied. Values for V_b of 0.15 and 0.25 ml are selected that are ± 0.05 ml off the minimum separation bubble volume of $V_{bmin} = 0.20$ ml. These maps are significantly different in character from the fixed frequency maps. For these tests low Q_g values imply low f. In Fig. 29 at low Q_g, single bubble separations are observed despite $V_b < V_{bmin}$ due to the capillary overshoot mechanism. Interestingly, these rarely complete separations do not appear to impact the ingestion limit, which steadily increases with increasing Q_g at a common slope provided $V_b \lesssim V_{bmin}$. The overshoot-coalescence phenomena ends with increases in Q_l and Q_g.

In Fig. 30, since $V_b > V_{bmin}$, the 100% separation condition for singles and mergers is the norm, though an island of mixed partial separation behaviour is evident. Though Figs. 29 and 30 represent the only true fixed bubble volume maps completed, binning bubble volume data within ± 0.0125 ml of select values, the regime map transitions can be observed from Fig. 31a for the data and regime map boundaries and from Fig. 31b for the regime boundaries and shaded regimes. Inspection of Fig. 31 identifies how various regimes grow and decay with V_b.

6.3 Fixed Bubble Frequency, Variable Channel Length ($L = 15, 25, 48$ mm)

The length of the channel plays a critical role in the ability of such conduits to separate bubbles. Shorter channels allow less time for bubbles $V_b > V_{bmin}$ to reach the free surface. They also support significantly higher base flow ingestion limits Q_{ling} further reducing the time available for cross flow bubble migration, free surface

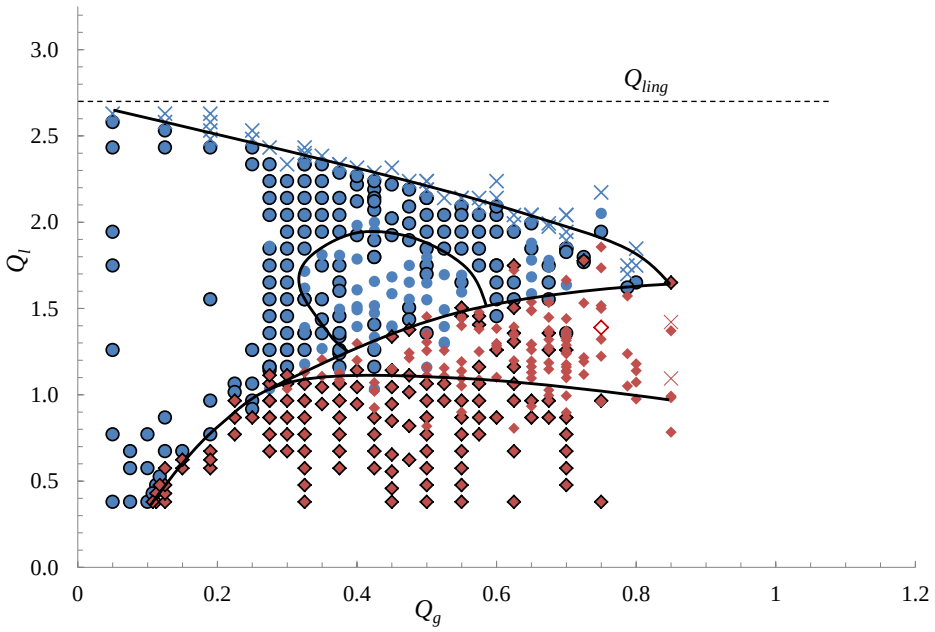

Figure 30. Regime maps for fixed bubble volume $V_b = 0.25$ ml.

coalescence, and separation. For a fixed frequency of $f = 1.25$ Hz, Figs. 32 and 33 present maps for free surface lengths $L = 15$ and 25 mm, respectively. The case of $f = 1.25$ Hz with $L = 48$ mm was presented in Fig. 25. The liquid flow rate at ingestion Q_{ling} varies with L and empirically determined values are identified in the figures along with Q_{gmin} (cf. Fig. 37). The 100% separation condition is achieved only in the case of mergers at low Q_l for the conditions established in these tests. Significantly higher Q_g values would be required for 100% for single bubbles to coalesce and exit. Particularly in Fig. 32, the shorter channel does not permit sufficient time for coalescence to occur. The shorter stiffer free surface also promotes the bouncing of larger bubbles, preventing coalescence within the free surface length L.

7 Examples of Data Reduction Directions

Various aspects of the general phenomena may be studied in greater depth using the video archive. Though efforts are continuing, we briefly address a few such topics here: merger transients and limits, bubble exit locations, and free surface wave dynamics.

7.1 Merge Transients and Approximate Limit Analysis

The large dataset is replete with bubble merger events of which only a subset will be touched on here. For example, a selection of 0% separation mergers are shown

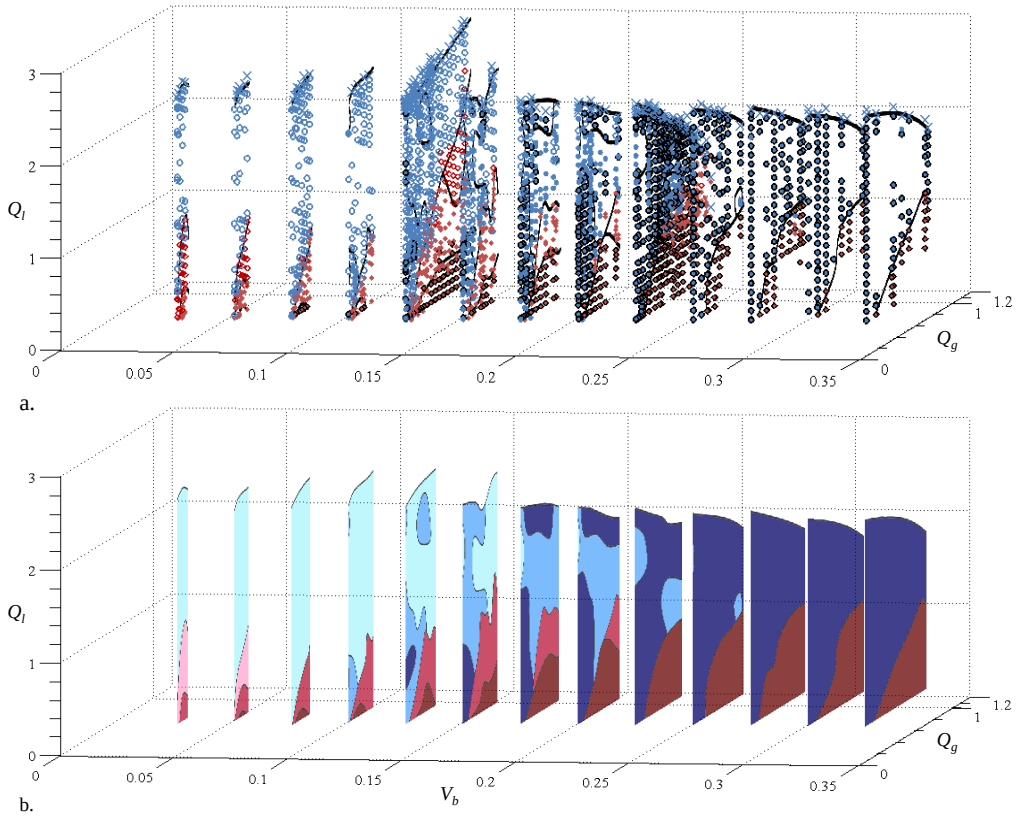

Figure 31. 3-D representation of regimes maps for constant bubble volume including data of Figs. 29 and 30: a. data with regime boundary sketch, b. shaded regimes. Values of V_b are provided ± 0.0125 ml for $V_b = 0.050$, 0.075, 0.10, 0.125, 0.15, 0.175, 0.20, 0.225, 0.25, 0.275, 0.30, 0.325, and 0.35 ml.

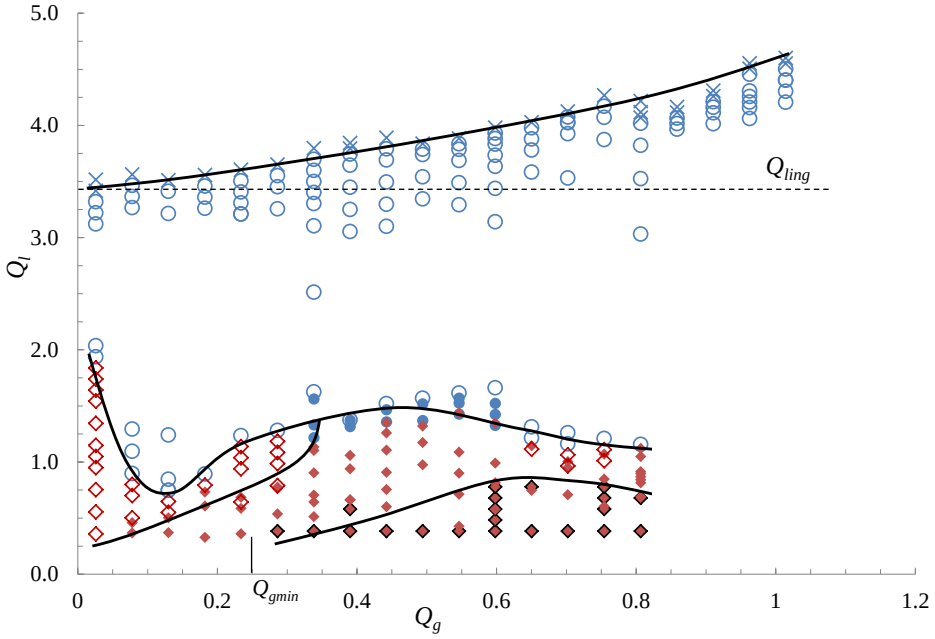

Figure 32. Regime map for fixed bubble frequency $f = 1.25$ Hz for free surface/slider length $L = 15$ mm with $Q_{ling} = 3.4$ ml/s. Compare also to Fig. 25 where $f = 1.25$ Hz and $L = 48$ mm.

in Fig. 34 with specific conditions listed. These are cases of pure channel exit mergers 34a, alternating bubble mergers 34b, pure channel entrance mergers 34c, and mixed mid-channel intermediate bubble volume mergers 34d. Other merger patterns are observed that could be defined to further subdivide the merger regime domains. For example, with generally increasing Q_g and Q_l we observe multi-mergers, several entrance merger types, pure mergers, harmonic mergers, sparse hydrodynamic mergers, and 100% singles with occasional mergers due to rebounds off the free surface. We restrict our attention here only to mergers resulting from over-packing bubble trains as typified in Fig. 34.

Merge dynamics are readily measured by digitizing the elevation of the top of the merged bubble $x_{bt}(t)$ for any merge event. This is accomplished in Fig. 35 for various 0% mergers varying V_b holding Q_l fixed, and holding V_b fixed while varying Q_l. A cursory inspection of the figure reveals that for this selection of conditions the migration velocity is nearly independent of V_b and Q_l, and that the initially slightly confined single bubbles are capable of only slightly overshooting their ideal merged bubble inscribed elevations x_{bti}, as was also demonstrated in the drop tower experiments in Fig. 3c-d. Note in this figure that for spherical bubbles $x_{bt} = x_b + R_b$, or $x_{bt} = R_b(1+\sin\alpha)/\sin\alpha$. From Fig. 35 the common migration rate of the merged bubbles is $\approx 6.4 \pm 0.4$ mm/s, which is significantly less than the common single bubble migration rate of $\approx 37.5 \pm 1.5$ mm/s from Fig. 5.

We note that for ideally inscribed single and merged bubbles, the merged bub-

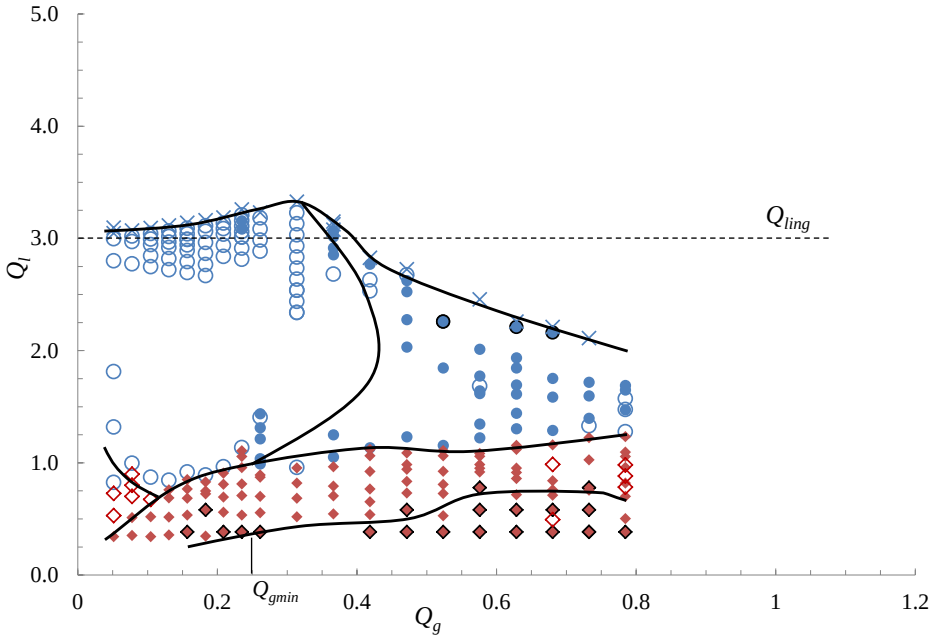

Figure 33. Regime map for fixed bubble frequency $f = 1.25$ Hz for free surface/slider length $L = 25$ mm with $Q_{ling} = 3.0$ ml/s. Compare also to Fig. 25 where $f = 1.25$ Hz and $L = 48$ mm.

ble occupies an elevation that should not interfere with other single bubbles if the distance between bubble surfaces satisfies

$$\delta_{rm} = \left(\frac{3V_b}{2\pi}\right)^{1/3} \left(\frac{1 - \sin\alpha - 2^{-1/3}(1 + \sin\alpha)}{\sin\alpha}\right) > 0, \tag{20}$$

where δ_{rm} is identified in Fig. 34b and d. The condition $\delta_{rm} = 0$ occurs when $\alpha = 6.6°$ (0.115 radians) and is independent of V_b. For wedge sections where $\alpha < 6.6°$, the merged bubbles may be expected to re-merge with other single bubbles at least once, whereas if $\alpha > 6.6°$, the merged bubble will move to an elevation that will not permit further interaction with other un-merged single bubbles. This conclusion emerges from the present study where $\alpha = 7.9°$, as observed in Fig. 34a and d, where the inertial capillary overshoot also works in favor of no re-merges. (The pure merger case of Fig. 34c has no chance to re-merge since all single bubbles merge.) However, re-mergers do occur as shown in Fig. 34b, suggesting that local hydrodynamics often trumps the simple inscribed bubble packing arguments presented here. Further details of re-mergers must be reported on a separate occasion.

Mergers are obviously increasingly likely with increasing bubble density. As the distance between bubbles decreases, any number of second order mechanisms can trigger the merge phenomena. A partial list of observed mechanisms includes: (1) variations in bubble volume and/or elevation, (2) pulsatile disturbances to the flow and free surface induced by subsequent bubble injections, (3) forward stagnation

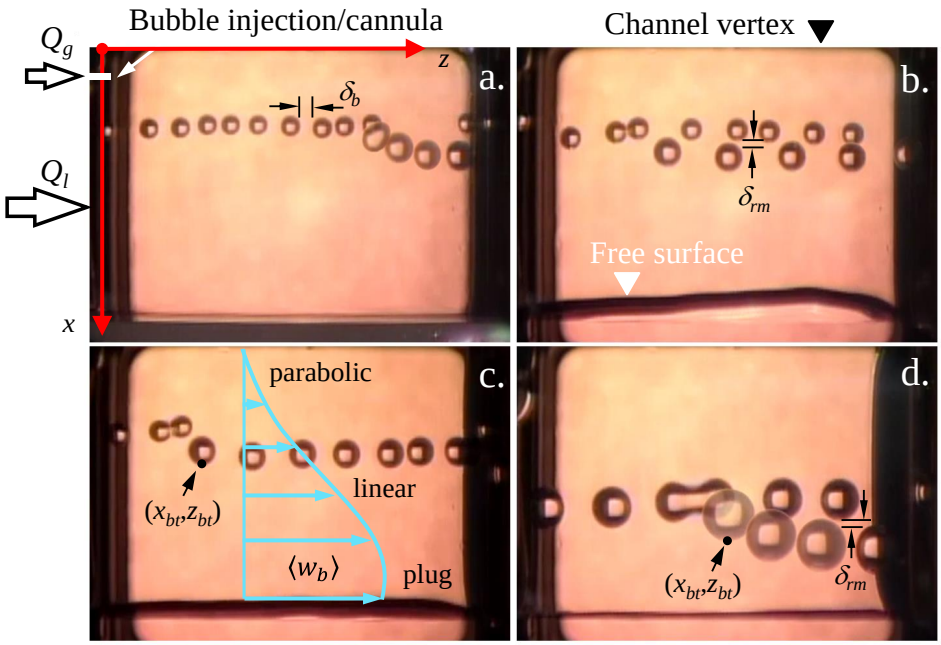

Figure 34. Examples of 0% separation bubble merger dynamics: a. 6 Hz images of mid-channel merger without re-merger for $f = 0.4$ Hz, $V_b = 0.007$ ml, $Q_l = 3.84$ ml/s, $Q_g = 0.0028$ ml/s, $L = 0$ mm; b. 3 Hz images of alternate bubble mergers where re-mergers do occur for $f = 3$ Hz, $V_b = 0.009$ ml, $Q_l = 2.61$ ml/s, $Q_g = 0.028$ ml/s, $L = 48$ mm; c. 3 Hz images of pure channel entrance mergers for $f = 3$ Hz, $V_b = 0.009$ ml, $Q_l = 2.36$ ml/s , $Q_g = 0.028$ ml/s, $L = 48$ mm; d. 3 Hz images of intermediate mid-channel mergers without re-mergers $f = 2$ Hz, $V_d = 0.055$ ml, $Q_l = 1.36$ ml/s, $Q_g = 0.111$ ml/s, and $L = 48$ mm. Approximate horizontal bubble separation δ_b, vertical re-merge bubble separation δ_{rm}, bubble top location x_{bt}, and 3-region velocity profile are identified as sketched.

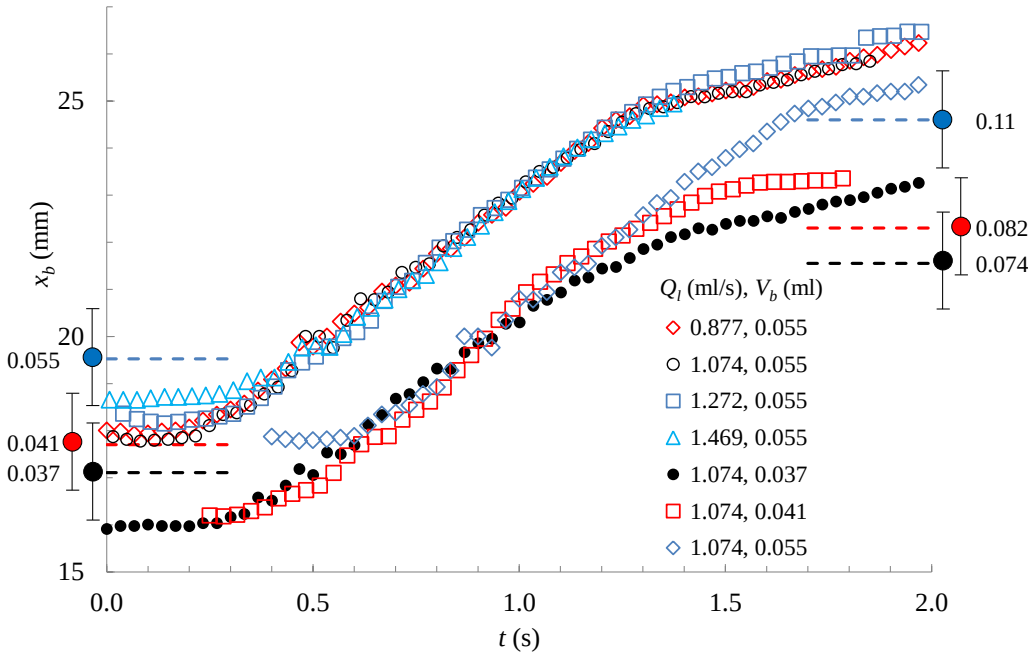

Figure 35. Bubble top surface elevation $x_{bt}(t)$ (ref. Fig. 34c-d) for mergers as functions of fixed V_b varying Q_l and fixed Q_l varying V_b. For these tests the single bubbles are slightly confined while the merged bubbles migrate slightly beyond their ideal inscribed elevations shown with approximate measurement uncertainties. The common slope is approximate by 6.4 ± 0.4 mm/s.

point flows generated by the capillary migration forcing previously injected bubbles ahead to merge with their predecessors, (4) entrainment of bubbles in adjacent bubble wakes, (5) unique flow harmonics, and (6) a channel exit contraction effect that can trip the merge phenomena from its densest bubble train condition, setting off a sequence of mergers that propagate upstream to the channel entrance where the bubble train is then gradually reestablished and the process repeated. Concerning variations in bubble volume, assuming that the bubbles take inscribed elevations, one might argue that any variation in V_b will ultimately lead to mergers, since larger bubbles move along slightly higher elevations where the base flow is faster enabling them to catch up and merge with any slightly smaller bubbles. Long channel lengths are likely to reveal additional details and an increased variety of merger phenomena. But the length of open capillary channels is limited by Q_{ling}. Such studies might best be conducted using closed channels as demonstrated in Fig. 34a.

Simple merge limit predictions are possible with knowledge of the critical bubble spacing δ_b and the base flow velocity profile $w_b(x_b)$, both of which are sketched in Fig. 34a for a train of bubbles with conditions specified. At steady state, the time period between bubble injections $(1/f)$ must equal the time required for a bubble to convect one bubble diameter plus the distance between bubbles δ_b, or

$$\frac{1}{f} = \frac{2R_b + \delta_b}{w_b}. \tag{21}$$

As suggested by bubble velocity plots such as Fig. 16 and from previous observations by [12], the developing velocity profile sketched in Fig. 34a consists of a parabolic boundary layer region near the vertex, a lengthy intermediate linear region potentially also in the boundary layer, and a plug flow-like free stream region near the free surface. The extent of each region depends primarily on the value of Q_l, the z-location, and free surface length L.

Assuming a vertex region parabolic profile of the form

$$w_b \approx \frac{4mQ_l}{H^2\alpha}\frac{x_b^2}{H^2}, \tag{22}$$

substituting into eq. 21 and solving for Q_l yields the low Q_g merge limit

$$Q_{lm1} \approx \frac{\alpha H^4 f}{4mx_b^2}(2R_b + \delta_b). \tag{23}$$

The ideal merge limit achieves $\delta_b = 0$ with fit coefficient m. Applying the geometric relationships $x_b \approx R_b/\alpha$ with $R_b = (3Q_g/4\pi f)^{1/3}$, eq. 23 becomes

$$Q_{lm1} \approx \frac{\alpha^3 H^4 f}{2m}\left(\frac{4\pi f}{3Q_g}\right)^{1/3}. \tag{24}$$

A value $m \approx 0.60 \sim O(1)$ will be shown to estimate the division between single and merged bubble regimes within the boundary layer in the near-vertex region of the flow.

Assuming an intermediate boundary layer region linear profile

$$w_b \approx \frac{nQ_l}{H^2\alpha}\frac{x_b}{H} - w_{bo}, \tag{25}$$

where w_{bo} is a velocity offset, substitution into eq. 21 and solving for Q_l yields a high Q_g merge limit

$$Q_{lm2} \approx \frac{\alpha^2 H^3 f}{nx_b}\left(f(2R_b + \delta_b) - w_{bo}\right). \tag{26}$$

Again, the ideal merge limit achieves $\delta_b = 0$ with fit coefficient n. Neglecting w_{bo} and applying $x_b \approx R_b/\alpha$ with $R_b = (3Q_g/4\pi f)^{1/3}$, eq. 26 reduces to the bubble volume-independent relationship

$$Q_{lm2} \approx \frac{2fH^3\alpha^2}{n}. \tag{27}$$

As will be shown, adequate estimates of the merger limit away from the vertex is achieved for $n = 3/2 \sim O(1)$. Theoretical and numerical hydrodynamic merge models are being considered, but the facility of the simple eqs. 24 and 27 will be demonstrated shortly in §8.

7.2 Bubble Exit length

Knowledge of the distance the bubble travels down the channel before coalescing with the free surface $z = l_H$ is an important metric for such flows since it permits one to determine the desired channel length to achieve a desired result. Data is recorded for the average value of l_{Hmeas} for 10 bubbles for 100% separation conditions. Only a single example is provided in Fig. 36 for fixed frequency $f = 0.75$ Hz and for the variety of bubble volumes specified. For inertial-capillary bubble migration ($Su_b^+ \equiv \rho\sigma V_b^{1/3}\alpha^{8/3}/\mu^2 \sim O(100)$) and inertial base liquid flows ($Re \equiv \rho Q_l/\mu H \sim O(100)$), the form suggested by [12]

$$l_H = C_f \frac{Q_l}{H}\left(\frac{\rho V_b^{1/3}}{2\sigma\alpha^{4/3}}\right)^{1/2} \tag{28}$$

is found to approximate the linear trends observed, where the fit coefficient for $f = 0.75$ Hz is 3.66 ± 0.32. [12] found $C_f \approx 10.5$ for $f = 0.2$ Hz. The strong dependence of C_f on f is indicative of the sensitivity of coalescence to the various oscillations of the system. A wide variety of outcomes due to bubble frequency effects, harmonics, bouncing, bimodal behaviour (where two l_H values arise for one test condition), and other free surface interactions are readily observed in the data archive but will not be discussed further herein. For $Q_l \lesssim 0.7Q_{ling}$, the value of l_H from eq. 28 serves as a reasonable prediction of the minimum channel length required to separate bubbles $\gtrsim V_{bmin}$. At higher values of Q_l eq. 28 becomes increasingly conservative as the free surface is deflected increasing inward enhancing bubble coalescence. We also observe that for short channels, when the 1-D free surface

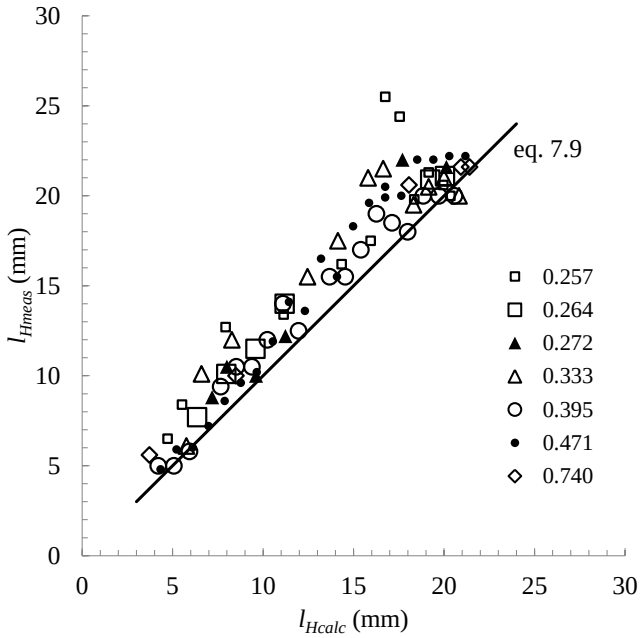

Figure 36. Measured bubble exit location l_{Hmeas} against calculated exit location l_{Hcalc} from eq. 28 with $C_f = 3.66$. For these tests bubble frequency is fixed at $f = 0.75$ Hz for the bubble volumes listed in ml.

curvature condition $(H\alpha/L)^2 \ll 1$ is not satisfied, the increased 'stiffness' of the free surface leads to significant rebounds that deny single bubbles a second opportunity to coalesce with the free surface before being swept through the channel exit. In such cases eq. 28 is inadequate.

7.3 Free Surface Wave Dynamics

Bubbles that coalesce at the free surface generate capillary waves with wavelength and speed tied to the bubble diameter and liquid flow rate Q_l. As expected, the smaller the bubble the faster the wave according to the well-known capillary wave dispersion relation $\omega^2 = \sigma k^3/\rho$, with wave angular frequency ω, wave number $k = 2\pi/\lambda$, and wavelength λ. Choosing $\lambda = 4R_b$, where R_b is the bubble radius, and defining capillary wave speed $w_{cwave} \equiv \lambda\omega$,

$$w_{cwave} \approx \left(\frac{\pi\sigma}{2\rho R_b}\right)^{1/2}. \tag{29}$$

For $V_{bmin} = 0.2$, $R_{bmin} = 3.6$ mm and for our tests we estimate $w_{cwavemin} = 66$ mm/s. Under-estimated as the average liquid velocity $\langle w \rangle$, the free surface velocity is

$$w_{FS} \approx \langle w \rangle \approx \frac{Q_l}{H^2 \tan\alpha}, \tag{30}$$

and for $Q_l = 1.86$ ml/s, $w_{FS} \approx 15$ mm/s is predicted. For comparisons, experiments for $Q_l = 1.86$ ml/s in Fig. 16 with an open slider show elevated velocities indicative of w_{FS} in the range of 20 mm/s.

The capillary waves propagate downstream at speeds equal to the capillary wave speed plus the free surface velocity—highs of 80 mm/s are observed for $Q_l = 1.86$ ml/s. Reflected waves return at speeds equal to the same capillary wave speed minus the free surface velocity—flows of 40 mm/s are observed from the data for $Q_l = 1.86$ ml/s. This general behaviour is estimated from the above approximations where $w_{wave} \approx w_{cwavemin} \pm w_{FS} = 66 \pm 15$ mm/s which compares well to terse observations of the data where 60 ± 20 mm/s. This approximate approach may be extended quickly to predict the time required for the wave produced by a bubble-free surface coalescence at $z = l_H$ to travel downstream a distance $L - l_H$, reflect, and return to location $z = l_H$ (ref. eq. 28). The time for this process is given by

$$t_r = \frac{L - l_H}{w_{cwave} + w_{FS}} + \frac{L - l_H}{w_{cwave} - w_{FS}} = \frac{2L(1 - l_H/L)}{w_{cwave}(1 - \Omega^2)}, \tag{31}$$

where $\Omega \equiv w_{FS}/w_{cwave}$. For the values of these experiments $\Omega = 0.227$, and for $Q_l = 1.86$ ml/s, from eqs. 29-31, $t_r \approx 1.07$ s. This 'reflection time' corresponds to a frequency $f_r = t_r^{-1} \approx 0.93$ Hz. This frequency for this flow rate is surprisingly close to the conditions identified by [12] (Fig. 15c in that article), where coalescence with the free surface could not be achieved at $f = 1$ Hz and $Q_l = 1.91$ ml/s. The present arguments support the claim that the natural frequency of the reflected waves match the bubble injection frequency f, providing a timely bounce to the free surface that prevents coalescence.

By such mechanisms the free surface waves can have local impact on coalescence and can set up harmonics within the system that retard or enhance bubble mergers and/or bubble coalescence. In general, however, the free surface waves serve as perturbations to the bubble paths and not as a primary mover, as can be gleaned from Figs. 15, 16, and 18, where bubble paths appear similar whether a free surface is present or not. Room is not afforded here to elaborate on such waves but their presence and impact is noted and may be pursued more quantitatively from the video archive.

8 Heuristic Regime Map

As guided by observations of the regime maps, simple heuristic models may be applied to predict the various regime boundaries observed and, as an example, we demonstrate approximate map construction for the fixed frequency case; i.e., Figs. 21-28. For our example, we will 're-construct' the $f = 1.25$ Hz map of Fig. 24 piecemeal by introducing each regime limit mechanism. Comparisons are then made to all experimental maps. We view this as a preliminary effort with anticipated improvements and generalizations following further analysis of the data and of subsequent third party theoretical and numerical work. In the meantime such capabilities are immediately of value for design.

8.1 Single Phase Liquid Ingestion Limit, Q_{ling}

The primary objective of the CCF experiments on ISS was to determine the single phase liquid ingestion limit Q_{ling} as a function of channel length L for three open channel geometries: parallel plate, rectangular groove, and wedge. These results are reported in detail elsewhere by [21] and [25]. The ingestion limit experimental data for the wedge channel is reproduced in Fig. 37. An image of the phenomena was presented in Fig. 7g. In general, Q_{ling} is computed by solving an approximate 1-D nonlinear ODE subject to CFD computed inlet boundary conditions. These results are included in Fig. 37. Additionally, to speed the assessment of designs and to rapidly compute this regime boundary for known channel length L, a closed form expression for this limit may be approximated by

$$Q_{ling} \approx \frac{\mu L}{2\rho\alpha^2}\left(\left(1+\frac{4}{3}\frac{\rho\sigma}{\mu^2}\frac{H^3\alpha^5}{L^2}\right)^{1/2}-1\right) \equiv \frac{\mu L}{2\rho\alpha^2}\left(\left(1+\frac{4}{3}Su^+\right)^{1/2}-1\right), \quad (32)$$

where $Su^+ \equiv (\rho\sigma H\alpha/\mu^2)(H\alpha^2/L)^2 \equiv Su(H\alpha^2/L)^2$ is a geometrically modified channel flow Suratman number Su that measures inertia in a visco-capillary flow. Su is essentially a Reynolds number based on the capillary velocity scale σ/μ. For the present tests, $0.015 \leq L \leq 0.048$ m and $100 \geq Su^+ \geq 10$. Eq. 32 may be inverted to predict critical channel length L_{ing} given liquid flow rate Q_l to find

$$L_{ing} \approx \frac{\sigma H^3\alpha^3}{3\mu Q_l}\left(1-\frac{3\rho Q_l^2}{\sigma H^3\alpha}\right). \quad (33)$$

Eqs. 32 and 33 are determined via scaling arguments that assume a narrow wedge $\alpha \ll 1$, dominant cross-channel curvature $(H\alpha/L)^2 \ll 1$, and an inertial-capillary flow that ingests once the contact line de-pins from the channel edge at the channel exit. Further details of the scaling arguments are provided in Appendix B. Eq. 32 along with a representation of its uncertainty $\sim Q_{ling}\cdot(1\pm(H\alpha/L)^2)$ is presented in Fig. 37. The error is $\lesssim 5\%$ for $L \geq 15$ mm. The observed agreement of the experiments with the upper uncertainty curve for the scale prediction is fortuitous. For the present study Q_{ling} for $L = 48$ mm is computed from eq. 32 and plotted on Fig. 38.

8.2 Minimum Gas Flow Rate For Separation, $Q_{gmin} = fV_{bmin}$

It has already been observed from the fixed frequency maps of Figs. 21-30 that single bubbles of radii larger than the maximum inscribed circle of the wedge section can be expected to reach the free surface, coalesce, and leave the flow. For the tangent bubble-free surface model shown in Fig. 20c we find

$$Q_{gmin} = fV_{bmin} \approx f\frac{4\pi}{3}\left(\frac{H\sin\alpha}{1+\sin\alpha}\right)^3. \quad (34)$$

A vertical line is drawn on Fig. 38 at this location and values of Q_g larger than this amount are expected to be increasing favorable to separation. It is also clear that single bubbles of volume $V_{bmin}/2$ that merge will then possess the minimum bubble

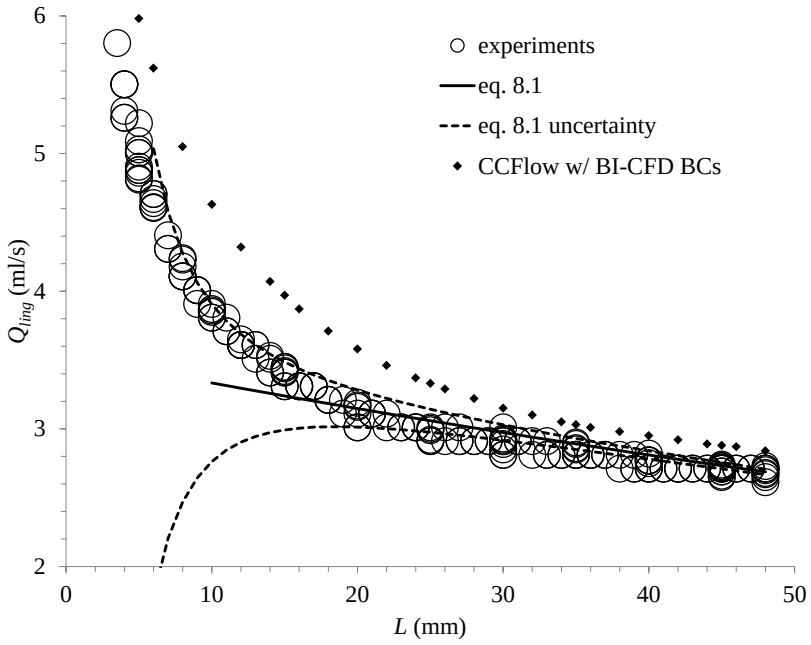

Figure 37. Single phase liquid flow limit above which the gas phase is ingested at the channel exit; i.e., the ingestion limit Q_{ling}. Experimentally determined values from [21] (symbols sized proportional to uncertainty) are provided with numerical predictions of [25] (dot-dash lines) and closed form scale predictions of eq. 32 (solid line) and expected uncertainty (dotted lined).

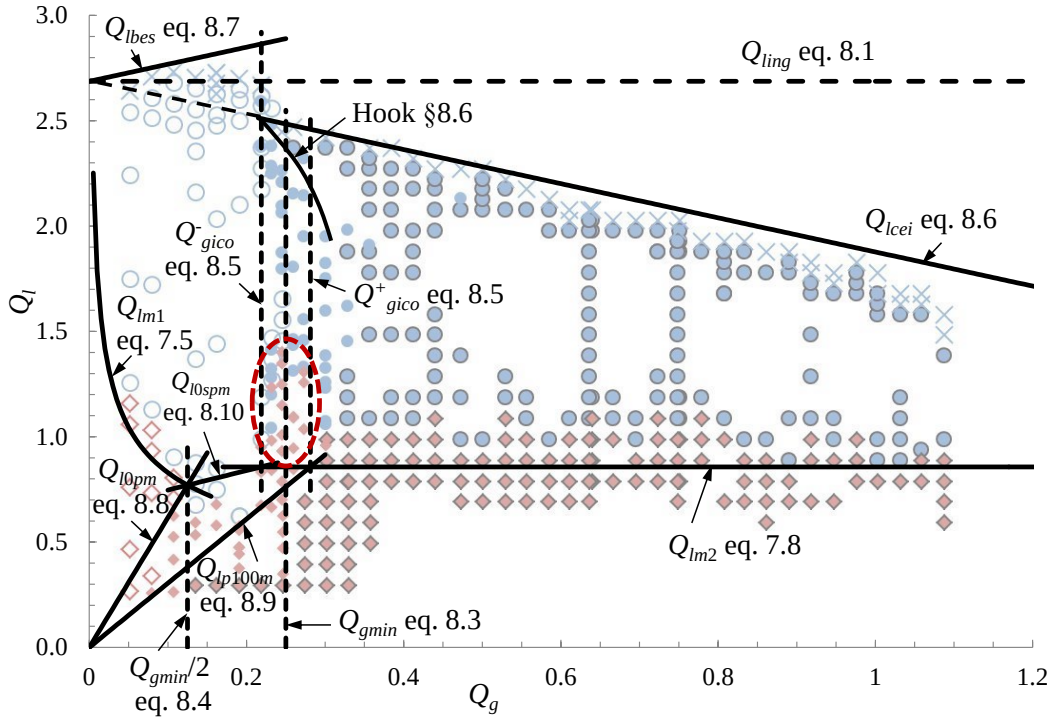

Figure 38. Example re-constructed fixed-frequency regime map. Each regime boundary lists the corresponding equation number. This map is constructed for the worst case condition of $f = 1.25$ Hz where discrepancies for $Qlbes$, Q_{lcei}, and Q_{lm2} are most apparent. Improved predictions are demonstrated in Fig. 39. The red dashed oval identifies the region of sparse hydrodynamic mergers not captured by the simple packing density approach of Q_{lm1} and Q_{lm2}.

volume required to reach the free surface. Thus, a dashed vertical line is drawn on the Fig. 38 at

$$Q_g = Q_{gmin}/2 \equiv f V_{bmin}/2. \tag{35}$$

8.3 Inertial Capillary Overshoot Limit, $Q^{\pm}_{gico}$

From observations of Figs 4, 14, and 15, due to the inertial-capillary bubble migration, bubbles can at times be propelled approximately 25% further than their ideal inscribed elevations. As a consequence, occasional partial single bubble separations are possible both below and above Q_{gmin}. The transition from 0% to 100% single bubble separations is therefore blurred and a region

$$Q_g = Q^{\pm}_{gico} \equiv Q_{gmin}(1 \pm 1/8) \tag{36}$$

does well to bracket the majority of outcomes, where the subscript *ico* refers to 'inertial-capillary overshoot.' Two vertical lines identify $Q^{\pm}_{gico}$ in Fig. 38.

8.4 Merge Limits

As briefly summarized in §7.1, small single bubbles within the boundary layer vertex region of the flow begin to merge below the liquid flow rate Q_{lm1} predicted by eq. 24 with $m = 0.60$. If the single bubble volume $V_b \lesssim V_{bmin}/2$, the merged bubble volume will remain below V_{bmin} and be unable to reach the free surface. However, if the single bubble volume $V_b \geq V_{bmin}/2$, the merged bubble volume will be $\geq V_{bmin}$ and such bubbles are capable of coalescing with the free surface. Thus, eq. 24 is plotted in Fig. 38 only up to the point it intersects with the vertical boundary associated with $Q_{gmin}/2$. This segment of eq. 24 is a vertex region merge limit where small single bubble mergers produce 0% separating mergers.

For larger bubbles that inscribe further away from the vertex, it was shown in Fig. 16 that the forced 'bubble velocity profile' is effectively linear. As developed in §7.1 for this situation, inscribed bubbles begin to merge for liquid flow rates below Q_{lm2} from eq. 27 with $n = 3/2$. Partial separations of single and merged bubbles within the $Q^{\pm}_{gico}$ band are expected with 100% merger separations expected for $Q_g \gtrsim Q^{+}_{gico}$. Thus, eq. 27 is plotted in Fig. 38 beginning from the point it intersects with the leftmost vertical boundary associated with Q^{-}_{gico}. This segment of eq. 27 represents a linear boundary layer flow region merge limit below which intermediate-to-large single bubble mergers are observed along with single bubble separations yielding what we define as partial and 100% separating mergers. As Q_g increases the percent of merging bubbles that coalesce with the free surface decreases compared to that of single bubbles that coalesce.

8.5 Bubble and Free Surface Coalescence Enhanced Ingestion Limit, Q_{lcei}

The common, apparently linear, bubble coalescence enhanced ingestion boundary (ref. line i., Fig. 6) begins for $Q_g > Q^{-}_{gico}$ and is found from the empirical maps to obey

$$Q_{lcei} \approx Q_{ling} - 0.81 Q_g. \tag{37}$$

Subscript *cei* denotes 'coalescence enhanced ingestion,' where bubbles coalescing with the free surface lower the ingestion (choking) limit of the liquid base flow at the channel exit. The case of $f = 1.25$ Hz yields an interesting outlier slope in eq. 37 of 1.02. A slope of ≈ 1 suggests that $Q_l + Q_g = Q_{ling}$ for $Q_g \gtrsim Q^-_{gico}$ and that the channel can never transport more combined volumetric flow rate than its maximum single liquid phase flow rate Q_{ling} when $Q_g \gtrsim Q^-_{gico}$. But the $f = 1.25$ Hz case is an outlier, which if included in the average would yield a slope of 0.85 ± 0.1. Ignoring it establishes 0.81 ± 0.07, which is presented in eq. 37. With knowledge of Q_{ling} from eq. 32, Q_{lcei} is computed from eq. 37 and plotted on Fig. 38 for $Q_g > Q^-_{gico}$.

8.6 The 'Hook' and the Bubble Enhanced Stability Regime

As described in §6, the Q^+_{gico} vertical boundary possesses a leftward hook as it nears the Q_{ling} limit. This hook approximately intersects with Q_{ling} and Q^-_{gico}, where it apparently triggers the end of the bubble enhanced stability regime (*bes*). Interestingly, within this regime the maximum value for $Q_l \equiv Q_{lbes} > Q_{ling}$ is correlated by

$$Q_{lbes} = Q_{ling} + 0.81 Q_g, \tag{38}$$

with an uncertainty in the slope of less than $\pm 2\%$. This value agrees with that of Q_{lcei} in eq. 37, but with opposite sign. Therefore the collapse of the bubble enhanced stability region decreases the liquid flow rate by $\Delta Q_l \approx 2 \cdot 0.81 Q^-_{lico}$. Eq. 38 is plotted and the hook is sketched in Fig. 38.

8.7 Analytical Map Comparisons and the Partial Merger Island

The merger regimes are complicated for Q_l values below the testable limits of the CCF hardware. The boundaries between 0% and partial mergers and partial and 100% mergers might be expected to emanate from the origin, the former intersecting with the terminus of the vertex region merge limit Q_{lm1} and the latter intersecting with Q^+_{gico} and free stream merge limit Q_{lm2}. Connecting the terminus of Q_{lm1} and the intersection of Q^-_{gico} with Q_{lm2} closes off the partial merger regime completing the map for practical purposes. The relationships for these boundaries are represented here by the following:
0% mergers to partial mergers ($0pm$)

$$Q_{l0pm} \equiv \frac{Q_{lm1}(Q_{gmin}/2)}{Q_{gmin}/2} \cdot Q_g = \frac{\alpha^3 H^4}{0.60} \left(\frac{8\pi}{3 V^4_{bmin}} \right)^{1/3} \cdot Q_g; \tag{39}$$

Partial mergers to 100% mergers ($p100m$)

$$Q_{lp100m} \equiv \frac{Q_{lm2}}{Q^+_{lico}} \cdot Q_g = \frac{2^5}{3^3} \frac{H^3 \alpha^2}{V_{bmin}} \cdot Q_g; \tag{40}$$

0% singles to partial mergers ($0spm$)

$$Q_{l0spm} \equiv Q_{lm2} + \frac{Q_{lm2} - Q_{lm1}(Q_{gmin}/2)}{Q^-_{gico} - Q_{gmin}/2} \cdot \left(Q_g - Q^-_{gico} \right)$$

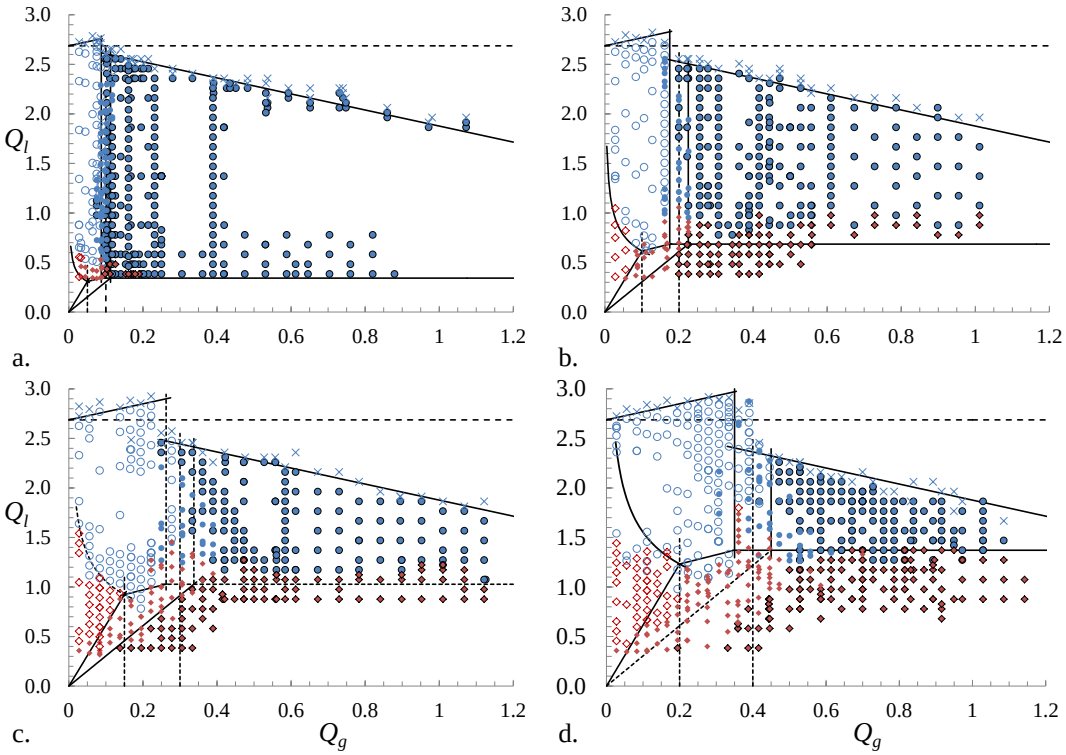

Figure 39. Fixed-frequency regime maps with calculated boundaries drawn: a. $f = 0.5$, b. 1.0, c, 1.5, and d. 2.0 Hz bubbles.

$$= Q_{lm2} + \frac{8\alpha^2 H^3}{3V_{bmin}} \left(\frac{4}{3} - \frac{\alpha}{0.60} \left(\frac{\pi H^3}{3V_{bmin}} \right)^{1/3} \right) \left(Q_g - Q^-_{gico} \right), \tag{41}$$

where Q_{lm2} and Q^-_{gico} are given by eqs. 27 and 36, respectively. Eqs. 39–41 are also plotted on Fig. 38 approximately enclosing the partial merger regime.

9 Discussion

All of the heuristic regime limits discussed in §8 and culminating in Fig. 38 are computed and plotted for comparisons to four of the fixed frequency regime maps in Fig. 39. The agreement is encouraging if not adequate. The best results are observed for Q_{ling}, Q_{lbes}, and Q_{lcei}, but taken together they allow one to quickly estimate expected performance for expected values of Q_g and Q_l. The worst result is the lack of prediction of the partial merges observed clustered near the bottom of the $Q^{\pm}_{gico}$ regime as identified by the red dashed oval in Fig. 38 and data of Fig. 39. After a closer look, these mergers occur for sparse bubbles where $\delta_b \gtrsim 2R_b$, well below the packing limits of §7.1 and are enabled by strong hydrodynamic interactions between bubble pairs. This additional class of sparse hydrodynamic mergers is

clearly identified by the fact that they do not conform to simple packing arguments. Observations point to bubble wake vertex interaction and entrainment complicated by a growing base flow boundary layer. Further investigation of such mechanisms is postponed for the time being.

From the §8 arguments, for similar systems ($\sim Su^+$) one is able to establish specific geometric dimensions, gas and liquid flow rates, and even margins of safety to prevent or ensure passive bubble separation in the open wedge conduit. For processes such as boiling, one must establish means to assess V_b distributions. But even a light inspection of the present results will greatly speed such efforts. These results compliment, but also significantly extend, the quantitative results of [12].

10 Conclusions

These CCF space experiments aboard the ISS employ an unusually large buoyancy-free 2-phase flow of bubbles driven along an open wedge channel. The experimental apparatus is configured to study the passive phase separating characteristics of the geometry providing a large database for further fundamental and applied investigations of the inertial capillary phenomena. The problem is of particular relevance to fluids management aboard spacecraft, but is also relevant for fast flows of low viscosity liquids in terrestrial applications. The space experiments conducted record thousands of events during 40 days of continuous commanding from ground stations and the $\sim O(1\text{TB})$ video archive is made publicly available on the internet for broader dissemination.

Enough important characteristics of the flow are gathered from inspection of the data combined with heuristic scaling arguments to provide a fair reconstruction of the flow regimes arising in such systems. Based on the importance of the inscribed bubble elevation, these include a priori design guides predicting minimum bubble volumes required to separate, or merge and separate, within the length of channel specified. The regime map is bounded above by a gas ingestion limit in a bubble enhanced stability region at low gas flow rate and a bubble-free surface coalescence enhanced ingestion region at moderate to high gas flow rates. Theoretical and numerical analyses can draw from the data set to investigate a variety of interesting aspects of the flow; such as the further division of the merger regimes (multi-mergers, entrance mergers, harmonics, etc.), merger hydrodynamics, the often retarding or enhancing effect of free surface waves on coalescence, the coupled hydrodynamics of the inertial cross-flow capillary migration with the inertial developing base flow, and the changes in bubble behaviour above and below the growing boundary layer within the flow—in particular, the long-time elevation of bubbles driven below or beyond their inscribed elevations due to the developing shear flow in the asymmetric channel. Such behaviours within fully-developed flows would be a practical first step. Further data reduction efforts are ongoing that include significant drop tower experimental results and numerical analysis. The CCF experiment hardware resides on the ISS and experiments are resumed in August 2014 and will be reported separately.

Appendix A

CCF EU2-02 Video Archive

The video archive for the 2nd (02) run of the Capillary Channel Flow (CCF) wedge Experiment Unit (EU2) is publicly available at http://psi.nasa.gov requiring only a request for access. It is referred to as CCF-EU2-02. The approximately 880 GB database contains the video results of over 5000 set points varying V_b, f, Q_l, and L. The files may be downloaded on a case by case basis or in total. The data is largely provided and referenced from a single Microsoft Excel spreadsheet with all critical experiment conditions listed and with each associated video hyper-linked. Fig. A40 provides an image of the spreadsheet that conveys the general format. The Excel file employs a variety of macros to sort the data and the most populated maps of Figs. 21-27 (fixed f), Figs. 29 and 30 (fixed V_b), and Figs. 32 and 33 (fixed L) are provided where one may select any data point in the plots to pull up the associated video. This 'hyper-linking' considerably facilitates the understanding of the general regime behaviour and is an enjoyable way to peruse the data.

For subsequent quantitative data reduction via image analysis, each video file must be rectified to correct for camera skew. Instruction and batch files are available in the archive to perform this operation. For indices of refraction $N_{Dquartz} = 1.458$ for the test channel and $N_{DHFE} = 1.29$ for the test liquid, for the wedge of $\alpha = 7.9°$ one determines that refraction effects are $\lesssim 0.3\%$ and may effectively be ignored if desired. Further instructions regarding the CCF-EU2-02 database are provided at http://psi.nasa.gov.

Appendix B

Q_{ling} Scale Analysis

A scale form for the z-component zero-gravity steady momentum equation is

$$\rho w w_z \sim -P_z, \mu \Delta w, \tag{B42}$$

where w is the imposed z-component of velocity, P_z is the free surface capillary under-pressure gradient along the channel, and Δ is the 2-D Laplacian operator in the x-y-plane. Subscript notation is employed for partial differentiation. Following the line of scaling arguments for corner flows taken by [26], [27], [23], and [12], in the narrow wedge limit $\alpha \ll 1$ with $\theta = 0$, and with negligible streamwise curvature $(H\alpha/L)^2 \ll 1$, choosing scales $w \sim \langle w \rangle \approx Q_l/h^2\alpha$, $P \sim -\sigma/h\alpha$, and $\Delta \sim 1/h^2 F_i \alpha^2$, eq. B42 is re-written as

$$-\frac{2\rho C_d Q_l^2}{h^5\alpha^2} h_z \sim -\frac{\sigma}{h^2\alpha} h_z, -\frac{\mu Q_l}{h^4 F_i \alpha^3}, \tag{B43}$$

where C_d is an $O(1)$ unknown inertial drag coefficient and F_i is an unknown $O(1)$ inverse viscous resistance coefficient—the larger F_i the lower the viscous resistance.

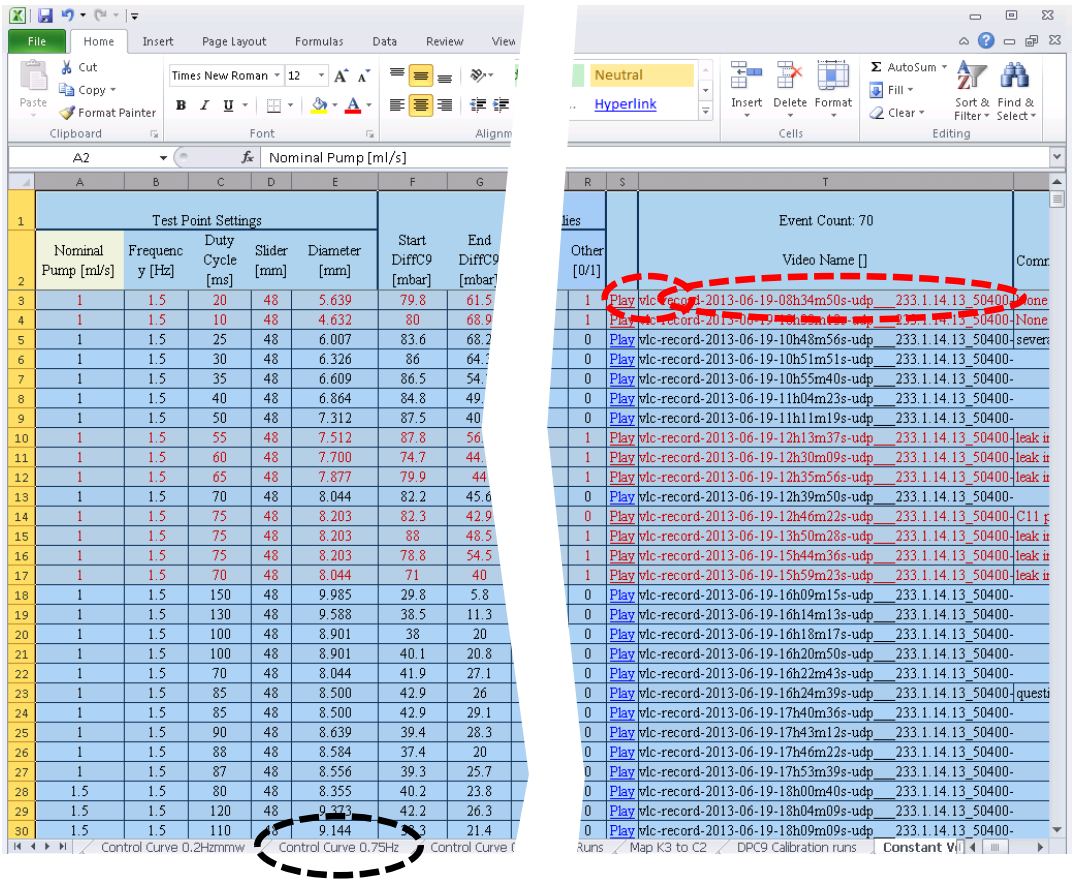

Figure A40. Sample screen shot from the CCF-EU02 data/video archive. Listed along with all of the most relevant test conditions is the video name identified by the large red dashed oval. Clicking the small red dashed oval brings up the video for the event. The most complete maps of Figs. 21–27 (fixed f), Figs. 29–30 (fixed V_b), and Figs. 32–33 (fixed L) are accessible from the tabs at the bottom of the file. For example, the black dashed oval identifies the location of the $f = 0.75$ Hz map, Fig. 23. Each data point of the maps is hyper-linked to the video record which is accessed by simply clicking the data point in question.

The negative sign on the viscous dissipation term is informed by the elliptic nature of the developing velocity field. By scaling quantities $h \sim H$ and $h_z \sim -H\alpha/L$, eq. B43 is converted to an algebraic expression

$$\frac{2\rho C_d}{H^4 L\alpha} Q_l^2 + \frac{\mu}{H^4 F_i \alpha^3} Q_l - \frac{\sigma}{HL} = 0, \tag{B44}$$

which when $C_d = 3/2$ and $F_i = 1/3$ is solved for Q_l or L presented in eqs. 32 and 33, respectively. For the fully developed vertex region of the flow $F_i = 1/6$ is expected, but this region contributes little to the overall flow rate and away from the vertex the wedge geometry may be modelled by nearly parallel walls where $F_i \approx 1/3$ is a better choice. The value $C_d = 3/2$ then brings about the agreement observed in Fig. 37.

Appendix C

Entrance Length Issues

A scale for the entrance length of the acute wedge duct may be estimated by balancing streamwise convection with cross flow viscous resistance such that

$$\frac{\rho}{2}\frac{\partial w^2}{\partial z} \sim \mu \Delta w, \tag{C45}$$

where Δ is the Laplacian operator. Substituting scales $z \sim z_e$, $w \sim Q_l/H^2 \tan\alpha$, and the Laplacian scale for the free surface case $\Delta \sim \Delta_s = 1/x_e^2 \sin^2\alpha$ ([27]) one obtains

$$\frac{\rho Q_l}{2 z_e H^2 \tan\alpha} \sim \frac{\mu}{x_e^2 \sin^2\alpha}, \tag{C46}$$

from which eq. 19 is found taking $\alpha \ll 1$. Subscript e denotes and entrance length quantity. Eq. 18 is found by setting $x_e = H$ and taking $\alpha \ll 1$. The enclosed conduit values are found by employing the hydraulic radius approach to estimate $\Delta_s = (1+\alpha)^2/x_e^2 \sin^2\alpha$. As a check on this approach note that for a circular cylindrical tube of radius $R = D/2$, $\Delta_s = 2/R^2$ and from eq. C45 one finds $L_e \sim DRe_D/16$. Despite the qualitative nature of such scaling arguments the coefficient $1/16$ is quite close to the accepted typical value of 0.06, [28].

References

1. V. Ajaev and G. Homsy, "Modeling shapes and dynamics of confined bubbles," *Annu. Rev. Fluid. Mech.*, vol. 38, pp. 277–307, 2006.

2. D. Legendre and J. Magnaudet, "The lift force on a spherical bubble in a viscous linear shear flow," *J. Fluid Mech.*, vol. 368, pp. 81–126, 1998.

3. B. Zhao, J. Moore, and D. Beebe, "Surface-directed liquid flow inside microchannels," *Science*, vol. 291, p. 1023, 2001.

4. J. Melin, W. van der Wijngaart, and G. Stemme, "Behaviour and design considerations for continuous flow closed-open-closed liquid microchannels," *Lab on a Chip*, 2005.

5. A. Skelleya and J. Voldmana, "An active bubble trap and debubbler for microfluidic systems," *Lab on a Chip*, August 2008.

6. J. Xu, R. Vaillant, and D. Attinger, "Use of a porous membrane for gas bubble removal in microfluidic channels: physical mechanisms and design criteria," *Microfluid Nanofluid*, March 2010.

7. T. John, *Investigation of microbubble/droplet formation in cross-flow and co-flow micro devices*. PhD thesis, Louisiana Tech University, 2011.

8. C. Litterst, S. Eccarius, C. Hebling, R. Zengerle, and P. Koltay, "Increasing ldmfc efficiency by passive co_2 bubble removal and discontinuous operation," *J. Micromech Microeng*, vol. 16, pp. 248–253, 2006.

9. R. Dangla, S. Kayi, and C. Baroud, "Droplet microfluidics driven by gradients of confinement," *PNAS*, vol. 110, pp. 853–858, January 2013.

10. T. Metz, N. Paust, R. Zengerle, and P. Koltay, "Capillary driven movement of gas bubbles in tapered structures," *Microfluidics and Nanofluidics*, vol. 9, pp. 341–355, April 2012.

11. E. Reyssat, "Drops and bubbles in wedges," *J. Fluid Mechanics*, 2014. (accepted for publication).

12. R. Jenson, A. Wollman, M. Weislogel, L. Sharp, R. Green, P. Canfield, J. Klatte, and M. Dreyer, "Passive phase separation of microgravity bubbly flows using conduit geometry," *Int. J. Multiphase Flow*, 2014. (submitted).

13. D. Wollman, "Capillarity-driven droplet ejection," Master's thesis, Portland State University, June 2012.

14. M. Weislogel, Y. Chen, S. Collicott, C. Bunnell, R. Green, and D. Bohman, "More handheld fluid interface experiments for the International Space Station (CFE-2)," No. AIAA-2009-0615 in 47th AIAA Aerospace Sciences Meeting, (Orlando), pp. 1–10, 2009.

15. W. Blackmore, M. Weislogel, Y. Chen, C. Bunnell, L. Kiewidt, and J. Klatte, "The Capillary Flow Experiments (CFE-2) aboard the ISS: Status," No. AIAA-2011-1196, (Orlando), pp. 1–10, 49th AIAA Aerospace Sciences Meeting, Jan. 2011.

16. M. Weislogel, J. Baker, and R. Jenson, "Quasi-steady capillarity driven flow," *J. Fluid Mechanics*, vol. 685, pp. 271–305, 2011.

17. L. Cheng, G. Ribatski, and J. Thome, "Two-phase flow patterns and flow-pattern maps: Fundamentals and applications," *Appl. Mech. Rev.*, vol. 61, p. 28 pages, July 2008.

18. A. Barajas and R. Panton, "The effects of contact angle on two-phase flow in capillary tubes," *Int. J. of Multiphase Flow*, vol. 19, no. 2, pp. 337–346, 1993.

19. R. Spivey, W. Sheredy, and G. Flores, "An overview of the Microgravity Science Glovebox (MSG) facility, and the gravity-dependent phenomena research performed in the MSG on the International Space Station (ISS)," No. AIAA-2008-0812., 46th AIAA Aerospace Sciences Meeting, 2008.

20. U. Rosendahl, A. Ohlhoff, and M. Dreyer, "Choked flows in open capillary channels: theory, experiment and computations," *J. Fluid Mech.*, vol. 518, pp. 187–214, 2004.

21. P. Canfield, P. Bronowicki, Y. Chen, L. Kiewidt, A. Grah, J. Klatte, R. Jenson, W. Blackmore, M. Weislogel, and M. Dreyer, "The capillary channel flow experiments on the international space station: Experiment setup and first results," *Experiments in Fluids*, vol. 54, pp. 1519–1532, 2013.

22. M. Weislogel, "Survey of present and future challenges in low-g fluids transport processes," *NASA Contract Report C-74461-N*, 2001.

23. J. Klatte, *Capillary flow and collapse in wedge-shaped channels.* PhD thesis, Universitaet Bremen, 2011.

24. P. Canfield, "Stabilization of free surface flow due to bubbly flows," 2014. in preparation.

25. M. Conrath, P. Canfield, P. Bronowicki, M. Dreyer, M. Weislogel, and A. Grah, "Capillary channel flow experiments aboard the international space station," *Physical Review E*, vol. 88, no. 063009, p. 8 pages, 2013. Rapid Communication.

26. M. Weislogel and S. Lichter, "Capillary flow in an interior corner," *J. Fluid Mech.*, vol. 373, pp. 349 – 378, 1998.

27. M. Weislogel, Y. Chen, and D. Bolledulla, "A better nondimensionalization scheme for slender laminar flows: The laplacian operator scaling method," *Phys. Fluids*, vol. 20, no. 2, pp. 163 – 170, 2008.

28. B. R. Munson, D. F. Young, and T. H. Okiishi, *Fundamentals of Fluid Mechanics.* New York: Wiley, fourth ed., 2002.